HHS Public Access

Author manuscript

Inorg Chem. Author manuscript; available in PMC 2017 January 19.

Published in final edited form as:

Inorg Chem. 2016 January 19; 55(2): 419–431. doi:10.1021/acs.inorgchem.5b01662.

Models of the Ni-L and Ni-SI_a States of the [NiFe]-Hydrogenase Active Site

Geoffrey M. Chambers[†,‡], **Mioy T. Huynh**[†], **Yulong Li**[†], **Sharon Hammes-Schiffer**[†,*], **Thomas B. Rauchfuss**[†,‡,*], **Edward Reijerse**, and **Wolfgang Lubitz**[*]

†

‡

Abstract

A new class of synthetic models for the active site of [NiFe]-hydrogenases are described. The $Ni^{I/II}(SCys)_2$ and $Fe^{II}(CN)_2CO$ sites are represented with $(RC_5H_4)Ni^{I/II}$ and Fe^{II}(diphos)(CO) modules, where diphos = 1,2-$C_2H_4(PPh_2)_2$(dppe) or *cis*-1,2-$C_2H_2(PPh_2)_2$(dppv). The two bridging thiolate ligands are represented by $CH_2(CH_2S)_2^{2-}$ (pdt^{2-}), $Me_2C(CH_2S)_2^{2-}$ (Me_2pdt^{2-}), and $(C_6H_5S)_2^{2-}$. The reaction of Fe(pdt)$(CO)_2$(dppe) and $[(C_5H_5)_3Ni_2]BF_4$ affords $[(C_5H_5)$Ni(pdt)Fe(dppe)-(CO)$]BF_4$ ([**1a**]BF_4). Monocarbonyl [**1a**]BF_4 features an $S = 0$ $Ni^{II}Fe^{II}$ center with five-coordinated iron, as proposed for the Ni-SI_a state of the enzyme. One-electron reduction of $[\mathbf{1a}]^+$ affords the $S = {}^1/_2$ derivative $[\mathbf{1a}]^0$, which, according to density functional theory (DFT) calculations and electron paramagnetic resonance and Mössbauer spectroscopies, is best described as a Ni^IFe^{II} compound. The Ni^IFe^{II} assignment matches that for the Ni-L state in [NiFe]-hydrogenase, unlike recently reported $Ni^{II}Fe^I$-based models. Compound $[\mathbf{1a}]^0$ reacts with strong acids to liberate 0.5 equiv of H_2 and regenerate $[\mathbf{1a}]^+$, indicating that H_2 evolution is catalyzed by $[\mathbf{1a}]^0$. DFT calculations were used to investigate the pathway for H_2 evolution and revealed that the mechanism can proceed through two isomers of $[\mathbf{1a}]^0$ that differ in the stereochemistry of the Fe(dppe)CO center. Calculations suggest that protonation of $[\mathbf{1a}]^0$ (both isomers) affords Ni^{III}–H–Fe^{II} intermediates, which represent mimics of the Ni-C state of the enzyme.

Graphical abstract

[*]Corresponding Authors: shs3@illinois.edu. rauchfuz@illinois.edu. wolfgang.lubitz@cec.mpg.de.

Notes

The authors declare no competing financial interest.

Supporting Information

The Supporting Information is available free of charge on the ACS Publications website at DOI: 10.1021/acs.inorg-chem. 5b01662. Experimental details, calculated reduction potentials, $\Delta\nu_{CO}$, a comparison of crystal and DFT-optimized structures using different DFT functionals, calculated relative free energies, barriers, and spin densities for all intermediates in the catalytic cycles, extended discussion of the Ni–Fe bond, discussion of the TS and isomerization for $[\mathbf{1a}]^+$ and $[\mathbf{1a}]^0$, and coordinates and energies of all optimized structures (PDF)

X-ray crystallographic data in CIF format (CIF)

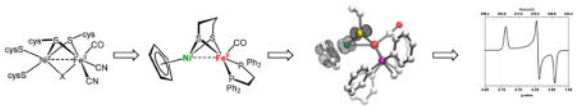

INTRODUCTION

Hydrogenases are enzymes that catalyze the oxidation of hydrogen and reduction of protons at high rates and low overpotentials, reactions that are potentially useful for clean energy applications.[1–4] Hydrogenases are classified into three main families according to the metals in their active site: [Fe]-, [FeFe]-, and [NiFe]-hydrogenases.[5,6] These enzymes are oxygen-sensitive but the [NiFe]-hydrogenases can recover from oxygen poisoning.[8,9] Model compounds have been useful in elucidating catalytic mechanisms or atom identity, notably with [FeFe]-hydrogenases.[7,10] [FeFe]-hydrogenase models are fairly advanced and have strong resemblance and relevance to the enzymatic system.[3,4,11] In contrast, models of the oxygentolerant [NiFe]-hydrogenases are less mature, and comparisons to the enzymatic system are sometimes less applicative.[3,4,12,13]

The [NiFe]-hydrogenase active site features a $[Ni(SCys)_4]^z$ center linked through two thiolate bridges to an $Fe(CN)_2(CO)$ center (Figure 1). In the absence of a third bridging ligand, the geometry at nickel resembles that of SF_4, while iron is square-pyramidal. The active states of the enzyme differ in three ways: (i) the oxidation state of the Ni center, (ii) the presence/absence of a hydride ligand bridging the two metals, and (iii) the state of protonation of at least one terminal cysteinyl thiolate. In contrast to the fluctuating oxidation states at the nickel center, iron appears to remain low-spin Fe^{II} throughout all of the known states of the enzyme active site.

Beyond complementing our understanding of the enzyme, synthetic models could underpin the development of new catalysts for the processing of H_2.[1,2] The possibility of connecting synthetic complexes to enzyme states was established with $[(dppe)Ni(pdt)(\mu\text{-}H)Fe(CO)_3]^{+}$.[14,21] A related nickel–iron hydride $[(amine)_2Ni(SR)_2(\mu\text{-}H)FeL_3]^{+}$ catalyzes the reduction of redox dyes by H_2, a characteristic assay for the hydrogenases.[15] With a Ni^{II}–H–Fe^{II} core, these synthetic complexes represent early models for the Ni-R state of the protein, despite discrepancies (Table 1).[16]

Concurrent with the development of these diamagnetic models,[21,22] efforts have been made to replicate the paramagnetic states of the enzyme. The two most prominent paramagnetic states are Ni-C and Ni-L. Invoked in all catalytic mechanisms is Ni-C,[6,7,23–25] which features a hydride bridging the Ni^{III} and Fe^{II} centers. No synthetic analogues of this nickel(III) hydride have been detected, but this paper provides a first glimpse of a synthetic model. With a $Ni^{I}Fe^{II}$ core, Ni-L is typically generated by low-temperature photolysis of Ni-C, and recent evidence points to its role in catalysis.[26,27] These $S = {}^1/_2$ states deviate most strongly from the conventional chemistry of dimetal systems and therefore offer the greatest opportunity for the discovery of fundamentally new reactivity. The first reported $S = {}^1/_2$ NiFe complex was $[(diphos)Ni(pdt)Fe\text{-}(CO)_2L]^{+}$. Spectroscopic, crystallographic, and computational analyses show, however, that these cations are described as $Ni^{II}Fe^{I}$

derivatives,[20,28] *not* $Ni^{I}Fe^{II}$ as assigned to the Ni-L state of the enzyme.[16] The lapse is a consequence of the $Fe(CO)_2L$ center, which stabilizes Fe^{I}. In the present report, the $Fe(CO)_2L$ center is replaced by the Fe(diphos)(CO) module, which more strongly stabilizes Fe^{II}.[22]

One of the weaknesses in the first generation of active-site model is a high reorganization energy upon oxidation at nickel.[21] This work addresses this weakness. Redox at the nickel centers typically induces changes in the coordination geometry, such that Ni^{I} species (cf. Ni-L) are tetrahedral and $Ni^{II/III}$ species (cf. Ni-SI_a, Ni-R, Ni-C) are square-planar (Figure 2). In contrast, the NiFe active site changes only subtly as it converts among catalytic states.[16,27] To minimize reorganizational barriers, the $[Ni(diphos)]^z$ site is replaced by $[(C_5H_5)Ni]^z$. The $[(C_5H_5)Ni(SR)_2]^z$ center has the advantage that its geometry is relatively insensitive to redox, in contrast to $Ni(dppe)(SR)_2$-based models (Figure 2). Not only does the hapticity of C_5H_5 not change, but crystallographic studies[29–31] show that the Ni-C_5H_5 distances are relatively invariant (<0.12 Å) for Ni^{I}, Ni^{II}, and $Ni^{III}(C_5H_5)$ compounds.

RESULTS AND DISCUSSION

Models for Ni-SI: Synthesis and Structure

The reaction of $Fe(pdt)(CO)_2(dppe)$ and $[(C_5H_5)_3Ni_2]BF_4$ in nitromethane affords $[(C_5H_5)Ni(pdt)Fe(dppe)(CO)]BF_4$ ([**1a**]BF_4; eq 1) as a dark-red powder. The derivatives $[(C_5H_5)Ni(pdt)Fe(dppv)$-$(CO)]BF_4$ ([**1b**]BF_4), $[(C_5H_5)Ni(Me_2pdt)Fe(dppe)(CO)]$-$BF_4$ ([**1c**]BF_4), and $[(CH_3C_5H_4)Ni(pdt)Fe(dppe)(CO)]BF_4$ ([**1d**]BF_4), where dppv = *cis*-1,2-$C_2H_2(PPh_2)_2$ and $Me_2pdt^{2-} = Me_2C(CH_2S^{-})_2$, were also prepared using the appropriate nickel and iron precursors. These salts are similar to [**1a**]BF_4 in terms of their reactivity and spectroscopic properties. The reaction of $Fe(pdt)(CO)_2(dppe)$ and $[(C_5H_5)_3Ni_2]BF_4$ proceeds via an intermediate with $\tilde{\nu}_{CO}$ = 1980 cm^{-1} that converts to $[\mathbf{1a}]^+$. We assign this intermediate band to the dicarbonyl complex *trans*-$[(C_5H_5)Ni(pdt)Fe(dppe)(CO)_2]$-$BF_4$. The disappearance of the intermediate band follows first-order decay (Figures S45 and S46). When the reaction progress is monitored by ^{31}P NMR spectroscopy, the iron precursor is consumed within ca. 5 min and two new singlet resonances are observed, one of which corresponds to the product $[\mathbf{1a}]^+$. Additionally, electrospray ionization mass spectrometry (ESI-MS) of the reaction mixture indicates the presence of the molecular cation $[(C_5H_5)Ni(pdt)Fe(dppe)$-$(CO)_2]^+$. These observations are consistent with the rapid attachment of "$(C_5H_5)Ni^+$" to the two isomers of the iron dithiolate. The *cis*-carbonyl derivative appears to release CO rapidly, whereas the isomer with *trans*-CO ligands is somewhat persistent.

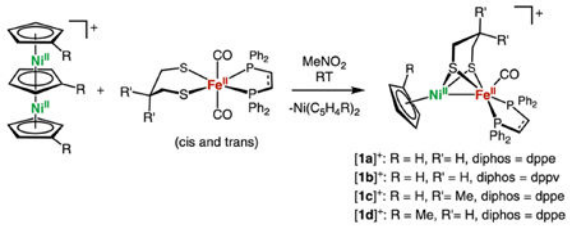

(1)

Purified compounds [**1a**–**1d**]BF_4 display a single $\tilde{\nu}_{CO}$ band in the range of 1940–1951 cm^{-1}, consistent with the presence of one isomer. These values are similar to those observed in Ni-SI_a, which range from 1927 to 1947 cm^{-1} (Table 2).[6]

The structure of [**1a**]$^+$ was confirmed by X-ray crystallography. The Ni–Fe distance is 2.5145(4) Å (Figure 3). Although the enzyme in the SI_a state has not been characterized crystallographically, it is generally assumed that the Ni–Fe distance is ~2.6 Å in all active states.[6] The stereochemistry of the $FeL_2(CO)$ site is biomimetic in the sense that CO occupies an apical site, and the two Lewis basic phosphine ligands are approximately trans to the sulfur centers of the thiolates.

The ^{31}P NMR spectra of complexes [**1a**–**1d**]BF_4 are simple, exhibiting only a single resonance, indicating chemically equivalent phosphorus centers or a dynamic process. The diphosphine in complexes [**1a**–**1d**]BF_4 is only observed in the dibasal arrangement, whereas other Fe(dithiolate)-(diphosphine)CO compounds have been shown to adopt both a dibasal and an apical–basal arrangement.[33] The phosphorus centers remain NMR-equivalent at −90 °C, suggesting either an exceptionally low barrier for isomerization or the presence of a single isomer. In the IR spectrum, only a single isomer is observed, which, like the enzyme's active site, has both donor ligands in basal positions.

The reaction of *cis*,*cis*-$Fe(SPh)_2(CO)_2$(dppv) and $[(C_5H_5)_3Ni_2]BF_4$ gave the dicarbonyl $[(C_5H_5)Ni(SPh)_2Fe$-(dppv)$(CO)_2]BF_4$ ([**2b**CO]BF_4), isolated as dark, almost black, microcrystals. Its ^1H NMR spectrum exhibits only one (C_5H_5) signal, and an AB quartet pattern in the ^{31}P NMR spectrum, indicating low symmetry. The structure was confirmed crystallographically (Figure S53). The Ni–Fe distance is 3.308(1) Å, indicating a noncovalent interaction. The stereochemistry at iron is identical with the precursor, wherein all ligands are cis. The μ-SPh groups are diaxial.

Upon treatment with Me_3NO, the dicarbonyl readily decarbonylated to give [**2b**]BF_4, isolated as a black solid. The IR spectrum of [**2b**]$^+$ in a CH_2Cl_2 solution displays a single $\tilde{\nu}_{CO}$ band at 1956 cm^{-1}, versus 2042 and 2002 cm^{-1} observed for the precursor. The monocarbonyl cation, [**2b**]$^+$, decomposes gradually in a CH_2Cl_2 solution. However, the complex is stable in MeCN, and the $\tilde{\nu}_{CO}$ band shifts 22 cm^{-1} to higher energies, suggesting the formation of an adduct. The ^{31}P NMR spectrum of [**2b**]$^+$ exhibits a singlet at δ 78.8. Under 1 atm of CO, MeCN solutions of [**2b**]$^+$ partially convert back to [**2b**CO]$^+$. In contrast, [**1a**]$^+$ is not reactive toward CO.

Electrochemistry

The cyclic voltammetry of [**1a**]BF_4 in dichloromethane (CH_2Cl_2) is very rich (Figure 4). Compounds [**1b**–**1d**]$^+$ produce similar voltammograms (Table 3). Compounds [**1a**–**1d**]$^+$ exhibit an irreversible oxidation near +0.65 V and a reversible one-electron reduction near −1.20 V, all versus $Fc^{0/+}$. Additionally, a quasi-reversible reduction is observed near −2.15 V, which becomes fully reversible when in tetrahydrofuran (THF) with $[Bu_4N]B(C_6H_3\text{-}3,5\text{-}(CF_3)_2)_4$ as the electrolyte. An irreversible reduction wave is generated at ca. 0.0 V versus $Fc^{0/+}$ following the irreversible oxidation.

The redox couples in the different derivatives are relatively similar. The reversible couple is most affected by Me_2pdt substitution. With $\Delta\tilde{\nu}_{CO}$ = 3 cm^{-1} (Table 1), the donor properties of pdt^{2-} and Me_2pdt^{2-} are similar in this system, and the difference in the potential of the $Ni^{II}Fe^{II}/Ni^{I}Fe^{II}$ redox couple may be due to the steric effects of the methyl groups. The reversible reduction in complexes [**1a**–**1d**]$^+$ shifts to more positive potentials by 50 mV upon replacement of (C_5H_5) for $CH_3C_5H_4$. This effect suggests that the reduction is nickel-centered, generating a $Ni^{I}Fe^{II}$ species. $CH_3C_5H_4$ substitution most affected the oxidation observed at ≈0.75 V, shifting this couple by −80 mV, whereas other substitutions only generate a 20–30 mV effect. This observation suggests that oxidation is nickel-centered. The reduction near −2 V is negligibly affected by the nickel-based ligands and is proposed to be an iron-centered reduction, generating a $Ni^{I}Fe^{I}$ species.

Density functional theory (DFT) was used to calculate the potentials associated with the couples [**1a**–**1d**]$^{2+/+}$, [**1a**–**1d**]$^{+/0}$, and [**1a**–**1d**]$^{0/-}$. The potentials were calculated relative to [**1a**]BF_4 and are provided in Table 3. The experimental trends are well reproduced by the calculations. The BF_4^- ions were not included in the calculations, which may cause deviations between the calculated and experimental values. The reduction potentials were also calculated for an alternative geometry optimization scheme, as well as using different functionals, and these results are provided in Tables S1 and S2.

Models for Ni-L: Synthesis and Structure

The reduced species [**1a**–**1d**]^0 and [**2b**]^0 were produced on a preparative scale by treatment with $(C_5H_5)_2Co$ (E^0 = −1.23 V; eq 2).

$$[(C_5H_5)Ni(SR)_2Fe(diphos)(CO)]BF_4 + (C_5H_5)_2Co \rightarrow (C_5H_5)Ni(SR)_2Fe(diphos)(CO) + [(C_5H_5)_2Co]BF_4 \quad (2)$$

Purified samples [**1a**–**1d**]^0 and [**2b**]^0 were isolated as black, air-sensitive solids. Reduction of [**1a**–**1d**]$^+$ and [**2b**]$^+$, a $Ni^{II}Fe^{II}/Ni^{I}Fe^{II}$ couple, shifts $\tilde{\nu}_{CO}$ by ca. 40 cm^{-1} to around 1900 cm^{-1}. A similar change is observed for the reduction of $[(dppe)Ni(pdt)Fe(CO)_3]^+$, a $Ni^{II}Fe^{I}/Ni^{I}Fe^{I}$ couple ($\Delta\tilde{\nu}_{CO} \approx 35$ cm^{-1} for this *tri*carbonyl).[20] Oxidation state changes centered at iron typically shift $\tilde{\nu}_{CO}$ by ca. 100 cm^{-1} as observed for $[(dppe)Pt(pdt)Fe(CO)_3]^{+/0}$, a $Pt^{II}Fe^{I}/Pt^{II}Fe^{0}$ couple.[21] For the Ni-L state of the [NiFe]-hydrogenases, the values of $\tilde{\nu}_{CO}$ range from 1911 (*Desulfovibrio vulgaris* Miyazaki F)[34] to 1862 cm^{-1} (*Aquifex aeolicus*) (Table 4).[26,35]

X-ray crystallographic analysis confirmed that the solid-state structures of [**1a**]^0 (Figure 5) and [**1a**]$^+$ (Figure 3) are very similar. The principal changes in these structures are in the coordination sphere of nickel, which suggests that the couple [**1a**]$^{+/0}$ involves a nickel-centered reduction. The Ni-C_5H_5 and Ni–S bonds elongate by about 5%, while the Fe–ligand bond lengths remain virtually unchanged. The Ni–Fe distance shortens by ~0.1 Å to 2.4593(5) Å, which is well within the sum of the atomic radii [2.56(6) Å], indicating the presence of metal–metal bonding. Although there are no crystallographic data on the metal–metal-bonded Ni-L state of the enzyme, DFT calculations predict this distance to be 2.56 Å.[36] The observed structural changes are consistent with reduction at the nickel center in the transformation of [**1a**]$^+$ to [**1a**]^0. The DFT-optimized structures of [**1a**]$^+$ and [**1a**]^0 were in excellent agreement with the crystal structures (Table 5).

DFT analysis of the spin density was used to determine the site of reduction of [**1a**–**1d**]$^+$. The plot of the spin density for [**1a**]^0 (Figure 6) reveals that the unpaired electron resides primarily on the nickel center, with some delocalization on the pdt^{2-} and $(C_5H_5)^-$ ligands but no significant delocalization on the iron. This result is consistent with the $Ni^{I}Fe^{II}$ assignment and the experimentally observed elongation of the Ni–ligand bonds upon reduction of [**1a**]$^+$.

The spin densities for the reduced species [**1a**–**1d**]^0 and [**2b**]^0 are given in Table 6 and consistently indicate a nickel-based reduction across all species. As observed for related nickel–iron dithiolate complexes,[20,21] the spin densities are not significantly affected by the conformation of the pdt ligand. Furthermore, the calculations also predict that an iron-based reduction would require potentials of 0.2–0.4 V more negative than the experimentally observed nickel-based reduction potentials (Table S1).

Crystallographic analysis revealed that the structure of [**2b**]^0 differs strongly from that of [**1a**]^0 (Figure 7). Specifically, the iron center is inverted such that the CO ligand is poised between the iron and nickel centers (eq 3). The CO ligand is not bridging, as indicated by the long Ni–CO distance of 2.878 Å. The DFT-optimized geometry of [**2b**]^0 is in good agreement with the crystal structure (Table S8), and the Ni–CO distance is calculated to be 2.916 Å. Furthermore, $\tilde{\nu}_{CO}$ for [**2b**]^0 is calculated to be 1911 cm^{-1} for the rotated structure, close to the observed value of 1915 cm^{-1}. A small shoulder at approximately 1900 cm^{-1} is also observed in the spectrum and may result from the presence of a second rotamer. For [**2b**]^0, the isomer in which the CO ligand is apical, as in the structure of [**2b**]$^+$, is calculated to be higher in free energy by 3.70 kcal mol^{-1} compared to the isomer in which the CO ligand is poised between the iron and nickel centers. This free energy difference is consistent with the crystal structure of [**2b**]^0 featuring an inverted iron center.

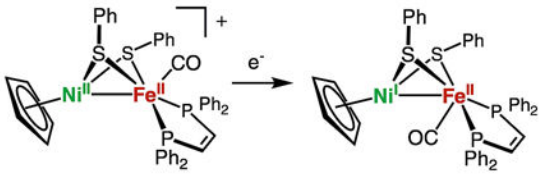

Models for Ni-L: Spectroscopy

The X-band continuous-wave electron paramagnetic resonance (CW-EPR) spectrum of [**1a**]^0 is rhombic with *g* values of 1.991, 2.042, and 2.138. No hyperfine coupling was detected (Figure 8). Spectra of [**1b**–**1d**]^0 are very similar to that of [**1a**]^0 (Table 7). The absence of significant ^{31}P hyperfine coupling is consistent with a nickel-centered radical, indicating that these compounds feature (C_5H_5)Ni^I centers. Large ^{31}P hyperfine coupling was observed in related mixed-valence compounds containing iron(I) phosphine centers, e.g., [$(CO)_2(PR_3)$Fe(pdt)Ni-(diphosphine)]$^{+}$.[20,28]

Q-band ENDOR experiments were conducted to probe the spin distribution in the mixed-valence state. Consistent with the absence of any hyperfine splitting in the EPR spectrum, the ^{31}P hyperfine couplings were found to be very small (~11 MHz; Table 8 and Figure S10). Several proton hyperfine contributions were detected using ENDOR spectroscopy with hyperfine splittings ranging from 4 to 11 MHz (Figure S9). The variant of complex [**1a**]^0 carrying C_5D_5 ([**1a**-d_5]^0) in place of C_5H_5 afforded a greatly simplified ^{1}H ENDOR pattern with the largest proton coupling (~11 MHz) being absent (Figure S8), indicating that the spin density is localized on the nickel and its immediate coordination sphere. The weaker ^{1}H couplings observed for [**1a**-d_5]^0 are assigned to two equivalent methylene protons of pdt^{2-}. These observations are consistent with DFT analysis, which shows that the spin density in [**1a**]^0 and [**2b**]^0 is primarily localized on the (C_5H_5)Ni(pdt) center (Figure 6 and Table 6). Despite the different stereochemistry at iron, at least in the solid state, and the presence of SPh$^-$ versus R_2pdt^{2-}, the EPR spectra of all mixed-valence compounds are similar.

The [**1a**-d_5]^0 orientation-selective ENDOR patterns (Figure S8) could be simulated with one proton hyperfine interaction (originating from two equivalent pdt^{2-} methylene protons). Although, in principle, up to eleven protons [C_5H_5 + $CH_2(CH_2S)_2$] could contribute to the ^{1}H ENDOR spectra of [**1a**]^0, only one additional contribution, assigned to the (C_5H_5) ligand, could be distinguished and evaluated (see Figure S9). It can be assumed that the proton(s) with their hyperfine tensors approximately aligned with the *g*-tensor axes lead to the strongest contributions along these axes in the orientation-selective ENDOR spectra. The hyperfine tensors of the C_5H_5 protons that are not aligned with the *g*-tensor axes give rise to additional weaker features in the ENDOR spectra (Figure S9), which have not been simulated. The simulation parameters of the $C_5H_5^-$ and pdt^{2-} (CH_2S) contributions are given in Table 8.

The measured Mössbauer spectra of [**1a**–**1c**]^0 and the corresponding cations are quite similar (see Figures S1–S6). All exhibit low isomer shifts of δ = 0.11–0.14 mm s^{-1} and small quadrupole splittings of ΔE_q = 0.72–1.15 mm s^{-1} (Table 9). The Mössbauer data are in agreement with a low-spin iron in all complexes. Consistent with other data in this paper, the spectra support the oxidation-state assignments of Ni^{II}Fe^{II} for compounds [**1a**–**1c**]BF_4 and Ni^{I}Fe^{II} for compounds [**1a**–**1c**]^0. The isomer shifts observed in the Ni^{I}Fe^{II} compounds [**1a**–**1c**]$_0$ are larger than the shift observed for the Ni^{II}Fe^{I} compound [(dppe)Ni(pdt)Fe$(CO)_3$]BF_4 (δ = 0.04 mm s^{-1}), while the quadrupole splittings are comparable (ΔE_q = 0.57).[20]

Mössbauer data for the [NiFe]-hydrogenases are sparse and suffer from difficulties in identifying and correcting for the dominating subspectra of the accessory FeS clusters.[37,38] Isomer shifts in the range of 0.05–0.15 mm s^{-1} have been assigned to the iron center of the [NiFe] center.[39]

The Mössbauer spectrum of [**1a**]^0 was further examined at high magnetic fields. This spectrum shows a very weak internal field contribution with an isotropic ^{57}Fe hyperfine coupling of 2 MHz (Table 8 and Figure S7). For comparison, magnetic Mössbauer spectra of the Fe^I center in the H_{ox} state of the [FeFe]-hydrogenase indicate ^{57}Fe hyperfine couplings in the range of 10–20 MHz.[40,41] The weak coupling is consistent with the spin being localized on the nickel center.

Electronic Structure Analysis

The geometries of the various species were optimized using DFT/BP86 and compared to the available experimental data to further probe the electronic structures of [**1a**–**1d**]$^+$ and [**1a**–**1d**]^0. The optimized geometries are in good agreement with the X-ray crystal structures. Relevant bond lengths for [**1a**]$^+$ and [**1a**]^0 are compared in Table 5. The BF_4^- counterions were not included in the geometry optimizations, which may introduce minor discrepancies between the X-ray crystal and DFT-optimized structures. Comparisons between the DFT and X-ray crystal structures for species [**1b**–**1d**]$^+$ and [**2b**]^0, as well as structural and energetic information for all systems studied, are provided in Tables S4–S8. Moreover, the CO stretching frequencies ($\tilde{\nu}_{CO}$) calculated with DFT are also in good agreement with the experimental data (Tables 2 and 4).

The short Ni–Fe distances in both [**1a**]$^+$ and [**1a**]^0 suggest the presence of metal–metal bonding interactions. According to previous analyses, such Ni–Fe bonds typically arise from overlap of the d_{z^2} orbitals.[21,42,43] Interestingly, however, the nature of the Ni–Fe bonding is quite different between [**1a**]$^+$ and [**1a**]^0, as revealed by analysis of the bonding molecular orbitals (MOs) localized using the Pipek–Mezey criteria.[44] For [**1a**]$^+$, the bonding orbital (Figure 9, left) reveals a dative Ni → Fe two-center, two-electron bond, which resembles a Lewis acid–base-type interaction between the d^8 Ni^{II} and d^6 Fe^{II} centers. In contrast, for [**1a**]^0, a more covalent two-center, two-electron bond is present (Figure 9, right), in which the Ni and Fe d_{z^2} orbitals contribute equally to the bonding orbital. An alternative bonding analysis using natural bond orbitals (NBOs)[45] is provided in the Supporting Information (pp S38–S40). The formation of a stronger σ bond in [**1a**]^0 is consistent with the experimentally observed contraction of the Ni–Fe bond distance from 2.51 Å in [**1a**]$^+$ to 2.46 Å in [**1a**]^0. This Ni–Fe bond-length contraction is also found in the DFT-optimized structures (Table 5). These chemical bonding patterns are similar for [**2b**]$^+$ and [**2b**]^0 (Figure S58), indicating that the stereochemistry at iron and the presence of SPh^- or R_2pdt^{2-} does not disrupt the Ni–Fe bond.

Protonation of Ni-L Model

Upon treatment with ≥1 equiv of acid, solutions of [**1a**]^0 liberate H_2 and afford the formation of [**1a**]$^+$ (eq 4).

$$\underset{[\mathbf{1a}]^0}{[(C_5H_5)Ni(pdt)Fe(CO)(dppe)]} + H^+ \rightarrow \underset{[\mathbf{1a}]^+}{[(C_5H_5)Ni(pdt)Fe(CO)(dppe)]^+} + \frac{1}{2}H_2 \quad (4)$$

H_2 evolution was observed for HBF_4, *p*-toluenesulfonic acid (pK_a^{MeCN} = 8.01), and [pyridinium]BF_4 (pK_a^{MeCN} = 12.33) but not for $[NH_4]PF_6$ (pK_a^{MeCN} = 14.46). With HBF_4, the yield of H_2 was 0.44 equiv, as assayed by gas chromatography. With [**1a**]^0 functioning as a one-electron reductant, 0.5 equiv would be predicted.

Protonolysis of [**1a**]^0 to give [**1a**]$^+$ entails the conversion of an $S = {}^1/_2$ precursor to an $S = 0$ product, which implicates a multistep process involving electron transfer. We anticipated that protonation of [**1a**]^0 would afford [(C_5H_5)Ni(pdt)HFe-(CO)(dppe)]$^+$ ([H**1a**]$^+$), a Ni^{III}–Fe^{II} species (see the DFT section below). However, hydrides were not obtained experimentally; rather, only [**1a**]$^+$ was obtained. To explain this result, [H**1a**]$^+$ is proposed to undergo reduction by its conjugate base [**1a**]^0, giving [H**1a**]^0, which, in turn, undergoes protonolysis to give [**1a**]$^+$. Similarly, we found that protonation of [**2b**]^0 afforded [**2b**]$^+$. The proposed sequence of reactions is summarized in Scheme 1.

Proposed H_2 Evolution Mechanism

In the presence of excess acid, [**1a**]$^{0/+}$ is a formal, albeit slow, electrocatalyst for H_2 evolution. Using trifluoroacetic acid, the catalytic current is observed at −1.16 V, corresponding to the [**1a**]$^{+/0}$ couple, with an acid-independent rate[46] of ca. 4 s^{-1} (Figure S32). Because the hydride intermediates could not be characterized, they were analyzed with DFT in the context of the mechanism for H_2 evolution. Additionally, the exclusive observation of the dibasal intermediate prompted theoretical investigation of an apical–basal isomer. These calculations provide insight into the structure and bonding of the nickel(III) hydride intermediate and also predict the occurrence of two parallel catalytic cycles involving isomers of [**1a**]^0. Similar bimetallic hydrides have been known to adopt different isomers.[22,47] Furthermore, recent work suggests that the protonation of (dppe)Ni(pdt)-$Fe(CO)_3$ proceeds via an unobserved isomer.[21]

According to the calculations, the dibasal and apical–basal isomers of [**1a**]^0 are nearly isoergic ($\Delta G°$ = +0.48 kcal mol^{-1}) and interconvert via a relatively low free energy barrier, $\Delta G^{\ddagger}$ = 11.76 kcal mol^{-1} (Table 11); however, all other protonation and oxidation states have a much higher barrier for isomerization (ΔG > 20 kcal mol^{-1}). This result prompted the investigation of two parallel pathways for H_2 evolution, labeled A and B in Figure 10.

These pathways are initiated by protonation of isomers of [**1a**]^0 that differ in terms of the stereochemistry of the (pdt)Fe(dppe)(CO) site. The adoption of the apical–basal isomer does not disrupt the Ni–Fe σ bond (Figure S56) or the localization of the unpaired spin density (Table 10 and Figure S57). The isomerization from the dibasal to the apical–basal configuration is expected to occur only for the [**1a**]^0 species because the calculated $\Delta G^{\ddagger}$ values for the analogous isomerization for all other intermediates in the catalytic cycle shown in Figure 10 are greater than 20 kcal mol^{-1} (Table 11). DFT analysis revealed that the transition state (TS) for this isomerization disrupts the metal–metal bonding (Supporting Information, p S41). For **[1a]**^{0}, the TS is best described as $Ni^{II}Fe^{I}$, while the TS is $Ni^{II}Fe^{II}$ in

[**1a**]$^{+}$. The lower isomerization barrier for [**1a**]^{0} is attributed to the greater stability of five-coordinated Fe^{I} compared to five-coordinated Fe^{II}.

The first step in the catalytic cycle produces isomers of [H**1a**]$^{+}$. In both isomers, the unpaired electron is localized mainly in the nickel coordination sphere (Table 10), indicating that these species are best described as $Ni^{III}HFe^{II}$, analogous to the Ni-C state in the enzyme. Moreover, the DFT-optimized structure of [H**1a**]$^{+}$ reveals that the hydride is more closely bound to iron than to nickel.

Subsequent to its formation, [H**1a**]$^{+}$ is reduced by a second 1 equiv of [**1a**]^{0} to form [**1a**]$^{+}$ and the nickel(II)–iron(II) hydride [H**1a**]^{0}. This electron transfer is proposed to occur spontaneously on the basis of the calculated reduction potential of [H**1a**]$^{+}$, which is less negative than the calculated reduction potential of [**1a**]$^{+}$ by 0.16 (cycle A) and 0.03 V (cycle B) versus $Fc^{+/0}$ in CH_2Cl_2. Reduction to form [H**1a**]^{0} mainly affects the nickel center and results in significant elongation of the Ni–H distance by 0.64 and 0.26 Å for the A and B isomers, respectively. Thus, [H**1a**]^{0}, which would be analogous to the Ni-R state of the enzyme, is more accurately described as a semiterminal iron(II) hydride than a bridging hydride.

The catalytic cycle closes with the protonation of [H**1a**]^{0} to produce the H_2-adduct intermediate, [H_2**1a**]$^{+}$, followed by the release of H_2 from [H_2**1a**]$^{+}$ to generate [**1a**]$^{+}$. Although the two cycles are very similar energetically, the calculations predict that this protonation is thermodynamically less favorable for the apical–basal isomer [H**1a**$^{\mathbf{B}}$]^{0} than for the dibasal isomer [H**1a**$^{\mathbf{A}}$]^{0} by ~5 kcal mol^{-1}.

In light of these computational results, additional experiments were performed to probe for the presence of two isomers in the catalytic cycle. The calculated $\tilde{\nu}_{CO}$ values for [**1a**$^{\mathbf{A}}$]^{0} and [**1a**$^{\mathbf{B}}$]^{0} are 1901 and 1904 cm^{-1}, respectively, and the calculated $\tilde{\nu}_{CO}$ values for [**1a**$^{\mathbf{A}}$]$^{+}$ and [**1a**$^{\mathbf{B}}$]$^{+}$ are 1946 and 1949 cm^{-1}, respectively. The calculated $\tilde{\nu}_{CO}$ values for all intermediates in the catalytic cycles are provided in Table S11. These small calculated $\tilde{\nu}_{CO}$ differences between the isomers are within the numerical accuracy of DFT. As previously mentioned, solutions of [**1a**]$^{+}$, which were synthesized directly, were confirmed crystallographically and spectroscopically to exist only in the dibasal geometry. However, the preparation of [**1a**]$^{+}$ by the addition of excess acid to [**1a**]^{0}, presumably going through the catalytic cycle(s) to generate H_2, produced a solution containing both isomers of [**1a**]$^{+}$. The ^{31}P NMR spectrum of the [**1a**]$^{+}$ solution obtained after presumably proceeding through the catalytic cycle(s) displayed two ^{31}P NMR signals, one assigned to the dibasal isomer (cycle A), in which the two ^{31}P centers are equivalent, and the other assigned to the apical–basal isomer (cycle B), in which the two ^{31}P centers are equilibrated by the rocking motion shown in Figure 11. The free energy barrier to this rocking motion is calculated to be relatively low, $\Delta G^{\ddagger}$ = 9.5 kcal mol^{-1}, and the ^{31}P NMR spectrum of the isomer mixture was unchanged when recorded at −100 °C, consistent with a relatively low free energy barrier. These analyses support the proposal that H_2 evolution can proceed via either cycle A or cycle B shown in Figure 10, thereby producing both isomers of [**1a**]$^{+}$.

CONCLUSIONS

Experiment and theory indicate that the new complexes reported in this paper replicate aspects of the following enzyme states: Ni-SI_a, Ni-L, Ni-C, and Ni-R. Two of these species, the $Ni^{II}Fe^{II}$ and $Ni^{I}Fe^{II}$ derivatives, were crystallized and fully characterized. The other two species are implicated in a H_2 evolution experiment and characterized computationally.

The Ni-SI_a state is distinguished by the $Ni^{II}Fe^{II}$ bimetallic core and the absence of a third bridging ligand, features that are replicated in compounds [**1a**–**1d**]BF_4. The Ni-L state is distinguished by the formal $Ni^{I}Fe^{II}$ oxidation states, a feature that is replicated in [**1a**–**1d**]^0. The oxidation state assignments are supported by EPR and Mössbauer spectroscopic data, crystallographic results, voltammetric measurements, and DFT calculations.

The previous attempts to model states with $Ni^{II}Fe^{II}$ cores suffered from the presence of six-coordinated iron centers.[17,48] The $Ni^{II}Fe^{II}$ models reported in this paper, in fact, arise via such $FeL_4(\mu\text{-}SR)_2$-containing intermediates, which undergo decarbonylation. DFT analysis of the bonding suggests that decarbonylation is driven by formation of the Ni–Fe bond. Although [**1a**–**1d**]$^+$ and [**2b**]$^+$ are reasonable spectroscopic models for the Ni-SI_a state of the enzyme, challenges remain. In the Ni-SI_a state, the nickel center binds CO to give Ni-SI_a^{CO}.[6,49] In contrast, [**1a**–**1d**]$^+$ exhibit no detectable affinity for CO. Substitution of the dithiolate bridge with bridging monothiolates, as in [**2b**]$^+$, facilitates the binding of CO at iron. In contrast, the enzyme binds CO at nickel. This difference is understandable because the $(C_5H_5)Ni(\mu\text{-}SR)_2$ site has a higher electron count than the $(RS)_2Ni(\mu\text{-}SR)_2$ site found in the enzyme. Replicating terminal thiolate ligation at nickel remains one of the central challenges in this area.[50]

The first attempts to model the mixed-valence active site of the Ni-L state focused on $[(CO)_2LFe(pdt)Ni\text{-}(diphosphine)]^+$.[20,28] These cations are described as $Ni^{II}Fe^{I}$, which is reversed from the $Ni^{I}Fe^{II}$ states assigned in Ni-L. More recently, we have characterized complexes with the configuration $Ni^{I}Ru^{II}$, wherein the Ru^{II} center is redox-inactive.[51] In this work, the $Fe(CO)_2(PR_3)$ center in previous Fe–Ni models was replaced by a $Fe(CO)(PR_3)_2$ center, which stabilizes the Fe^{II} state, as illustrated by [**1a**–**1d**]^0 and [**2b**]^0.

Because they are substrates, hydrogenic ligands are a major focus in research concerning the hydrogenases and their models.[52,53] The DFT-optimized analysis of the nickel(III)–iron(II) hydride [H**1a**]$^+$ reveals that the unpaired electron is localized mainly in the nickel coordination sphere, as seen for Ni-C. In the model, the hydride ligand is more closely bound to iron than to nickel [Δ(M–H) ~ 0.2 Å]. This report is the first suggestion of the accessibility of such a state in [NiFe]-hydrogenase model complexes. In the enzyme, proton-transfer reactions are coupled to electron-transfer reactions,[16] and a similar effect is seen in the reduction of [H**1a**]$^+$ by [**1a**]^0. The resulting nickel(II)–iron(II) hydride [H**1a**]^0, analogous to the Ni-R state of the enzyme, reacts with proton sources to liberate H_2. Although thwarting efforts to isolate this hydride, this facile protonolysis is analogous to the behavior of the Ni-R/Ni-SI pair.[16] According to our calculations, the nickel(II)–iron(II) hydride is more accurately described as a terminal iron(II) hydride than a bridging hydride. In contrast, high-resolution X-ray crystallographic analysis of Ni-R from *D. vulgaris* reveals Ni–H and

Fe–H distances of 1.58 and 1.78 Å (error 0.08 Å), respectively; i.e., the hydride is more closely associated with nickel.[16] The structural difference between the model complex and the protein may reflect the influence of terminal thiolate ligands on nickel.[50]

EXPERIMENTAL SECTION

Reactions and manipulations were performed using standard Schlenk techniques at room temperature or in a nitrogen atmosphere glovebox. Solvents were HPLC-grade and dried by filtration through activated alumina or distilled under nitrogen over an appropriate drying agent. Bu_4NPF_6 (GFS Chemicals, Columbus, OH) was recrystallized multiple times from a CH_2Cl_2 solution by the addition of hexane. Chromatography was performed using Siliflash P60 from Silicycle (230–400 mesh). ESI-MS data for compounds were acquired using a Waters Micromass Quattro II spectrometer. ^{1}H NMR spectra (500 MHz) were referenced to residual solvent relative to tetramethylsilane. $^{31}P\{^1H\}$ NMR spectra (202 MHz) were referenced to external 85% H_3PO_4. Fourier transform infrared (FT-IR) spectra were recorded on a PerkinElmer 100 FT-IR spectrometer. Crystallographic data for compounds [**1a**]^0, [**1c**]^0, [**2b**]^0, and [**2b**]BF_4 were collected using a Siemens SMART diffractometer equipped with a Mo Kα source (λ = 0.71073 Å), and crystallographic data for compounds [**1a**]BF_4 and [**1d**]BF_4 were collected using a Bruker D8 Venture diffractometer equipped with a Mo Kα microfocus source and a Photon 100 detector. X-band EPR spectra were recorded on a Varian E-line 12″ Century Series X-band continuous-wave spectrometer. Q-band ENDOR spectra were recorded on a Bruker Elexsys E580 Q-band pulse EPR spectrometer using a home-built pulse Q-band ENDOR resonator[54] and an ENI 300L RF amplifier. Cryogenic temperatures were achieved using a Cryogenic Ltd. closed-cycle cryostat. ENDOR simulations and spectral fits were performed using EasySpin ("salt")[55] and home-written scripts in *Matlab*. Mössbauer spectra were recorded on an alternating constant-acceleration spectrometer. The minimum experimental line width was 0.24 mm s^{-1} (full width at half-maximum). The sample temperature was maintained constant in either an Oxford Variox or an Oxford Mössbauer-Spectromag cryostat. The latter is a split-pair conducting magnet system for applying fields of up to 8 T to the samples that can be kept at temperatures in the range 1.5–250 K. The field at the sample is perpendicular to the γ-ray beam. Isomer shifts are quoted relative to metallic iron at 300 K. Mössbauer spectra were simulated with a home-written spin-Hamiltonian program based on the usual nuclear Hamiltonian formalism.[37]

$[(C_5H_5)_3Ni_2]BF_4$, $[(MeC_5H_4)_3Ni_2]BF_4$, and $[(C_5D_5)_3Ni_2]BF_4$

In a modification of Werner's procedure,[56] a solution of nickelocene (2.08 g, 11.0 mmol) in Et_2O (150 mL) was treated dropwise with an excess of $HBF_4{\cdot}Et_2O$ (2 mL, 13.8 mol). Over the course of several minutes, a purple solid precipitated from a pale yellow solution. The solid was collected by filtration and washed thoroughly with ether. Yield: 2.07 g (95%). ^{1}H NMR (nitromethane-d_3): δ 5.48 (10H, s), 4.80 (5H, s). $^{13}C\{^1H\}$ NMR (nitromethane-d_3): δ 87.8, 56.6.

[(C5H5)Ni(pdt)Fe(dppe)(CO)]BF4 ([1a]BF4)

To a solution of $[(C_5H_5)_3Ni_2]BF_4$ (498 mg, 1.24 mmol) in CH_3NO_2 (50 mL) was added a solution of Fe(pdt)(dppe)$(CO)_2$[22] (771 mg, 1.25 mmol) in CH_3NO_2 (25 mL). After 30 min, the slurry converted to a dark-red solution. Solvent was removed under reduced pressure, and the residue was washed several times with pentane until the filtrate was colorless. The residue was extracted into a minimal volume of CH_2Cl_2 and subjected to column chromatography. Byproducts elute with 100% CH_2Cl_2. The product eluted with 90:10 CH_2Cl_2/THF as a dark-red band. The solvent was removed under reduced pressure to yield a dark-red solid. Yield: 841 mg (85%). ^{1}H NMR (acetone-d_6): 8.01 (m, 4H), 7.5 (m, 16H), 4.75 (s, 5H, C_5H_5), 3.83 (m, 2H, PCH_2CH_2P), 3.62 (m, 2H, PCH_2CH_2P), 2.83 (m, 3H), 2.43 (m, 2H), 1.66 (m, 1H, $S_2CH_2CH_2CH_2S_2$). ^{31}P{^{1}H} NMR (acetone-d_6): δ 77.1. ESI-MS: *m*/*z* 711 ($[M]^+$), 683 ($[M - CO]^+$). IR (CH_2Cl_2): $\tilde{\nu}_{CO}$ 1943 cm^{-1} (THF). Anal. Calcd for $C_{35}H_{35}FeNiOP_2S_2$ (found): C, 52.61 (52.67); H, 4.42 (4.70). Single crystals of [**1a**]BF_4 were obtained by vapor diffusion of pentane into THF solutions.

[(C5H5)Ni(pdt)Fe(dppv)(CO)]BF4 ([1b]BF4)

Compound [**1b**]BF_4 was prepared in a fashion similar to that of [**1a**]BF_4 using Fe(pdt)(dppv)$(CO)_2$[22] as the iron reagent. Yield: 66%, dark-red powder. ^{1}H NMR (CH_2Cl_2): δ 8.44 (m, 2H, PC*H*C*H*P), 7.91 (br, 4H), 7.54 (s, br, 4H), 7.45 (s, br 12H), 4.31 (s, 5H, C_5H_5), 2.77 (m, 3H) 2.36 (m, 2H), 1.69 (m, 1H, $S_2CH_2CH_2CH_2S_2$). ^{31}P{^{1}H} NMR (CH_2Cl_2): δ 83.8. ESI-MS: *m*/*z* 709 ($[M]^+$), 681 ($[M - CO]^+$). IR (CH_2Cl_2): $\tilde{\nu}_{CO}$ 1951 cm^{-1}.

[(C5H5)Ni(Me2pdt)Fe(dppe)(CO)]BF4 ([1c]BF4)

Compound [**1c**]BF_4 was prepared in a fashion similar to that of [**1a**]BF_4 using Fe(Me_2pdt)(dppe)$(CO)_2$[22] as the iron source. Yield: 77%, dark-red powder. ^{1}H NMR (CH_2Cl_2): δ 7.77 (m, 4H), 7.46 (m, 16), 4.46 (s, 5H, C_5H_5), 3.65 (m, 2H, PCH_2CH_2P), 3.11 (m, 2H PCH_2CH_2P), 2.71 (m, 2H, $S_2CH_2CMe_2CH_2S_2$), 2.17 (m, 2H, $S_2CH_2CMe_2CH_2S_2$), 1.50 (s, 3H, $S_2CH_2CMe_2CH_2S_2$), 1.19 (s, $S_2CH_2CMe_2CH_2S_2$). ^{31}P{^{1}H} NMR (CD_2Cl_2): δ 75.1. ESI-MS: *m*/*z* 739 ($[M]^+$), 711 ($[M - CO]^+$). IR (CH_2Cl_2): $\tilde{\nu}_{CO}$ 1940 cm^{-1}. Single crystals of [**1c**]BF_4 were obtained by evaporation of concentrated THF solutions.

[(CH3C5H4)Ni(pdt)Fe(dppe)(CO)]BF4 ([1d]BF4)

Compound [**1d**]BF_4 was prepared in a similar fashion to [**1a**]BF_4 using the $[(CH_3C_5H_4)_3Ni_2]BF_4$ as the nickel source and Fe(pdt)(dppe)$(CO)_2$ as the iron source. Yield: 81%, dark-red powder. ^{1}H NMR (CH_2Cl_2): δ 7.80 (br, 4H) 7.52 (br, 4H) 7.43(br, 12H), 4.67 (br, 1H) 3.91 (br, 1H), 3.82 (s, 3H), 3.43 (m, 2H, PCH_2CH_2P), 3.05 (m, 2H, PCH_2CH_2P), 3.05 (m, 3H), 2.31 (m, 2H), 1.89 (br, 2H), 1.75 (m, 1H, $S_2CH_2CH_2CH_2S_2$). ^{31}P{^{1}H} NMR (CD_2Cl_2): δ 79.2. ESI-MS: *m*/*z* 725 ($[M]^+$), 697 ($[M - CO]^+$). IR (CH_2Cl_2): $\tilde{\nu}_{CO}$ 1943 cm^{-1}.

[(C5D5)Ni(pdt)Fe(dppe)(CO)]BF4 ([1a]BF4-d5)

Compound [**1a**]BF_4-d_5 was prepared in a fashion similar to that of [**1a**]BF_4 using $[(C_5D_5)_3Ni_2]BF_4$ as the nickel source. The product was characterized by ESI-MS, which indicated >95% deuteration (see the Supporting Information).

$Fe(SPh)_2(CO)_2(dppv)$

This compound was synthesized in a fashion similar to that of the published procedure.[57] To a mixture of $FeSO_4{\cdot}7H_2O$ (1.112g, 4.0 mmol) and dppv (1.584 g, 4.0 mmol) in MeOH (80 mL) was added dropwise a solution of PhSNa (1.056 g, 8.0 mmol) in MeOH (20 mL) with stirring under the presence of CO. After stirring for 6 h at room temperature, the solvent was removed under reduced pressure. The residue was extracted with CH_2Cl_2 (40 mL). After filtration to remove Na_2SO_4, the extract was concentrated (15 mL) and diluted with hexane (50 mL). Cooling this mixture at −20 °C for 12 h gave a red solid. Yield: 2.23 g (77%). ^{1}H NMR (CD_2Cl_2): δ 6.85–8.03 (32H, m). $^{31}P\{^1H\}$ NMR (CD_2Cl_2): δ 81.9 (d, J = 55 Hz), 61.1 (d, J = 55 Hz). IR (CH_2Cl_2): $\tilde{\nu}_{CO}$ 2023, 1978 cm^{-1}.

$[(C_5H_5)Ni(SPh)_2Fe(dppv)(CO)_2]BF_4$ ($[2bCO]BF_4$)

To a solution of $[(C_5H_5)_3Ni_2]BF_4$ (200 mg, 0.5 mmol) in CH_3NO_2 (15 mL) was added a solution of $Fe(SPh)_2(dppv)(CO)_2$ (364 mg, 0.5 mmol) in CH_3NO_2 (10 mL). After 30 min, the slurry converted to a dark-red solution. Solvent was removed under reduced pressure, and the residue was washed with pentane until the filtrate was colorless. The residue was extracted into a minimal volume of CH_2Cl_2 and subjected to column chromatography. After eluting impurities with 100% CH_2Cl_2, the product eluted with 90:10 CH_2Cl_2/THF as a dark-red band. The solvent was removed under reduced pressure to yield a dark-red solid. Yield: 380 mg (81%). ^{1}H NMR (CD_2Cl_2): δ 6.85–8.57 (32H, m), δ 4.46 (5H, s). $^{31}P\{^1H\}$ NMR (CD_2Cl_2): δ 75.9 (d, J = 45 Hz), 64.2 (d, J = 45 Hz). ESI-MS: m/z 849 ($[M]^+$), 821 ($[M - CO]^+$), 793 ($[M - 2CO]^+$). IR (CH_2Cl_2): $\tilde{\nu}_{CO}$ 2042, 2002 cm^{-1}. Anal. Calcd for $C_{45}H_{37}BF_4FeNiO_2P_2S_2{\cdot}CH_2Cl_2$ (found): C, 54.05 (53.69); H, 3.85 (3.72). Single crystals of [**2b**CO]BF_4 were obtained by solvent diffusion of pentane into CH_2Cl_2 solutions.

$[(C_5H_5)Ni(SPh)_2Fe(dppv)(CO)]BF_4$ ($[2b]BF_4$)

To a solution of [**2b**CO]BF_4 (280 mg, 0.3 mmol) in CH_2Cl_2 (30 mL) was added $Me_3NO{\cdot}2H_2O$ (34 mg, 0.3 mmol). After 1 h, the solvent was removed under reduced pressure, and the residue was washed several times with pentane. The residue was extracted into a minimal volume of CH_2Cl_2 (5 mL), pentane (30 mL) was added, and the mixture was cooled to −20 °C. The product was collected as a black powder. Yield: 200 mg (74%). $^{31}P\{^1H\}$ NMR (CD_2Cl_2): δ 78.8. ESI-MS: m/z 821 ($[M]^+$), 793 ($[M - CO]^+$). IR (CH_2Cl_2): $\tilde{\nu}_{CO}$ 1956 cm^{-1}. Anal. Calcd for $C_{44}H_{37}BF_4FeNiOP_2S_2{\cdot}0.5CH_2Cl_2$ (found): C, 56.16 (56.08); H, 4.02 (4.19).

$(C_5H_5)Ni(pdt)Fe(dppe)(CO)$ ($[1a]^0$)

To a stirred solution of [**1a**]BF_4 (21.2 mg, 26.5 μmol) in THF (3 mL) was added cobaltocene (5.8 mg, 30.7 μmol) in THF (3 mL). The solution immediately darkened, and solid $[(C_5H_5)_2Co]BF_4$ precipitated. The solvent is removed under reduced pressure, and the product was extracted into toluene (2 mL). The slurry was filtered through diatomaceous earth to yield a homogeneous, brown-black solution. The product is crystallized upon the addition of pentane (15 mL). Yield: 17.0 mg (90%), black powder. Single crystals were obtained by vapor diffusion of pentane into concentrated toluene solutions. IR (CH_2Cl_2):

$\tilde{\nu}_{CO}$ 1901 cm^{-1}. Anal. Calcd for $C_{35}H_{35}FeNiOP_2S_2$ (found): C, 59.02 (58.72); H, 4.95 (4.65).

$(C_5H_5)Ni(pdt)Fe(dppv)(CO)$ ($[\mathbf{1b}]^0$)

Compound $[\mathbf{1b}]^0$ was prepared in a fashion similar to that of $[\mathbf{1a}]^0$. Yield: 86%, black powder. IR (CH_2Cl_2): $\tilde{\nu}_{CO}$ 1903 cm^{-1}.

$(C_5H_5)Ni(Me_2pdt)Fe(dppe)(CO)$ ($[\mathbf{1c}]^0$)

Compound $[\mathbf{1c}]^0$ was prepared in a fashion similar to that of $[\mathbf{1a}]^0$. Yield: 87%, black powder. IR (CH_2Cl_2): $\tilde{\nu}_{CO}$ 1897 cm^{-1}.

$(CH_3C_5H_4)Ni(pdt)Fe(dppe)(CO)$ ($[\mathbf{1d}]^0$)

Compound $[\mathbf{1d}]^0$ was prepared in a fashion similar to that of $[\mathbf{1a}]^0$. Yield: 80%, black powder. IR (CH_2Cl_2): $\tilde{\nu}_{CO}$ 1898 cm^{-1}.

$(C_5D_5)Ni(pdt)Fe(dppe)(CO)$ ($[\mathbf{1a}\text{-}d_5]^0$)

Compound $[\mathbf{1a}\text{-}d_5]^0$ was prepared in a fashion similar to that of $[\mathbf{1a}]^0$.

$(C_5H_5)Ni(SPh)_2Fe(dppv)(CO)$ ($[\mathbf{2b}]^0$)

Compound $[\mathbf{2b}]^0$ was prepared in a fashion similar to that of $[\mathbf{1a}]^0$. Yield: 61%, black powder. IR (CH_2Cl_2): $\tilde{\nu}_{CO}$ 1915 cm^{-1}. Single crystals of $[\mathbf{2b}]^0$ were obtained by vapor diffusion of pentane into concentrated toluene solutions.

COMPUTATIONAL METHODS

DFT results reported herein were performed using the BP86 density functional.[58,59] Additional benchmarking was performed using the B3P86,[58,60] BP86-D2,[58,59,61] M06-L,[62] and ωB97XD[61,63–65] functionals and is presented in Tables S1–S7. The DFT calculations were performed with the Stuttgart pseudopotential and associated basis set of Preuss and co-workers (SDD)[66] for the nickel and iron centers, the 6-31G** basis set[67] for the μ-hydrogen ligand, and the 6-31G* basis set[68,69] for all other atoms. The starting geometries for $[\mathbf{1a}–\mathbf{1d}]^+$, $[\mathbf{1a}]^0$, and $[\mathbf{2b}]^0$ were obtained from their respective crystal structures. The starting coordinates for species without crystal structures were obtained by manual alteration of the most closely related crystal structure. Solvation free energies were calculated in CH_2Cl_2 using the conductor-like polarizable continuum model (C-PCM)[70,71] with the Bondi atomic radii[72] and including the nonelectrostatic contributions of dispersion,[73,74] repulsion,[73,74] and cavitation energies.[75]

For the results presented in the main paper, geometry optimizations were performed in the gas phase. However, geometry optimizations were also performed in solution and were found to be consistent with the gas-phase optimizations. A comparison of the structures optimized in the gas and solution phases is provided in Tables S4–S7. In all cases, the minimum-energy structures were confirmed to have no imaginary frequencies. The $\tilde{\nu}_{CO}$ frequencies were calculated within the harmonic model. Typically, DFT is more reliable for calculating changes in the frequencies than the absolute frequencies, and often scaling

factors dependent on the functional are used.[76] Herein, however, the absolute $\tilde{\nu}_{CO}$ values are reported because the BP86 functional gives excellent agreement with the experimental values without the application of scaling factors. Nonetheless, $\Delta\tilde{\nu}_{CO}$ values calculated using different functionals are provided in Table S3. The TSs for isomerization of the Fe(dppe)(CO) subunit were identified using the synchronous transit-guided quasi-Newton method,[77,78] and the TSs were confirmed to have only one imaginary frequency. Each TS was verified to lead to the relevant dibasal or apical–basal isomers by following the intrinsic reaction coordinate using the local quadratic approximation[79,80] for 5–10 steps in the forward and reverse directions and subsequently optimizing the geometries.

Thermochemical data were calculated at T = 298.15 K. All calculated free energies included zero-point energy, entropic contributions, and solvation effects. The reaction free energies ($\Delta G°$) and free energy barriers ($\Delta G^{\ddagger}$) associated with isomerization of the Fe(dppe)(CO) subunit in solution were calculated from the optimized geometries and TSs. The relative reduction potentials were calculated from the corresponding reaction free energies using a methodology described elsewhere.[81–84] Chemical bonding analysis was performed using the Pipek–Mezey localization criteria,[44] using keyword IOp(4/9=20212), and NBOs.[45] All calculations were performed using the *Gaussian 09* electronic structure program.[85] Structures and energies of the systems studied herein are provided in Tables S12–S73.

Supplementary Material

Refer to Web version on PubMed Central for supplementary material.

Acknowledgments

The synthesis work was supported by the National Institutes of Health through Grant GM061153 and the International Center of Carbon-Neutral Energy Research. We thank Bernd Mienert for the Mössbauer measurements and Dr. Eckhard Bill for insight into their interpretation. We also thank Katharina Weber for help with sample preparation and preliminary DFT calculations. The computational portion of this work was funded by the National Science Foundation Graduate Research Fellowship Program under Grant DGE-1144245 (to M.T.H.) and by the National Science Foundation Center for Chemical Innovation under Grant CHE-1305124. We thank Dr. Danielle Gray for assistance with the X-ray crystallographic analysis.

References

1. Bullock RM, Appel AM, Helm ML. Chem Commun. 2014; 50:3125.
2. Wang M, Chen L, Sun L. Energy Environ Sci. 2012; 5:6763.
3. Lansing, JC.; Manor, BC.; Rauchfuss, TB. Encyclopedia of Inorganic and Bioinorganic Chemistry. Scott, RA., editor. John Wiley; Chichester, U.K: 2014.
4. Schollhammer, P.; Weigand, W., editors. Bioinspired Catalysis. Wiley-VCH; Weinheim, Germany: 2014.
5. Frey M. Chem Bio Chem. 2002; 3:153.
6. Lubitz W, Ogata H, Rüdiger O, Reijerse E. Chem Rev. 2014; 114:4081. [PubMed: 24655035]
7. Tard C, Pickett CJ. Chem Rev. 2009; 109:2245. [PubMed: 19438209]
8. Parkin A, Sargent F. Curr Opin Chem Biol. 2012; 16:26. [PubMed: 22366384]
9. Wulff P, Day CC, Sargent F, Armstrong FA. Proc Natl Acad Sci U S A. 2014; 111:6606. [PubMed: 24715724]
10. Berggren G, Adamska A, Lambertz C, Simmons TR, Esselborn J, Atta M, Gambarelli S, Mouesca JM, Reijerse E, Lubitz W, Happe T, Artero V, Fontecave M. Nature. 2013; 499:66. [PubMed: 23803769]

11. Carroll ME, Barton BE, Rauchfuss TB, Carroll PJ. J Am Chem Soc. 2012; 134:18843. [PubMed: 23126330]
12. Ohki Y, Tatsumi K. Eur J Inorg Chem. 2011; 2011:973.
13. Chiou TW, Liaw WF. C R Chim. 2008; 11:818.
14. Barton BE, Rauchfuss TB. J Am Chem Soc. 2010; 132:14877. [PubMed: 20925337] Manor BC, Rauchfuss TB. J Am Chem Soc. 2013; 135:11895. [PubMed: 23899049]
15. Ogo S, Ichikawa K, Kishima T, Matsumoto T, Nakai H, Kusaka K, Ohhara T. Science. 2013; 339:682. [PubMed: 23393260]
16. Ogata H, Nishikawa K, Lubitz W. Nature. 2015; 520:571. [PubMed: 25624102]
17. Jiang J, Maruani M, Solaimanzadeh J, Lo W, Koch SA, Millar M. Inorg Chem. 2009; 48:6359. [PubMed: 20507106]
18. Krämer T, Kampa M, Lubitz W, van Gastel M, Neese F. Chem Bio Chem. 2013; 14:1898.
19. Kampa M, Lubitz W, van Gastel M, Neese F. JBIC, J Biol Inorg Chem. 2012; 17:1269. [PubMed: 23053531]
20. Schilter D, Nilges MJ, Chakrabarti M, Lindahl PA, Rauchfuss TB, Stein M. Inorg Chem. 2012; 51:2338–2348. [PubMed: 22304696]
21. Huynh MT, Schilter D, Hammes-Schiffer S, Rauchfuss TB. J Am Chem Soc. 2014; 136:12385. [PubMed: 25094041]
22. Carroll ME, Chen J, Gray DE, Lansing JC, Rauchfuss TB, Schilter D, Volkers PI, Wilson SR. Organometallics. 2014; 33:858. [PubMed: 24803716]
23. De Lacey AL, Fernández VM, Rousset M, Cammack R. Chem Rev. 2007; 107:4304. [PubMed: 17715982]
24. Siegbahn PEM, Tye JW, Hall MB. Chem Rev. 2007; 107:4414. [PubMed: 17927160]
25. Wu H, Hall MB. C R Chim. 2008; 11:790.
26. Hidalgo R, Ash PA, Healy AJ, Vincent KA. Angew Chem, Int Ed. 2015; 54:7110.
27. Greene BL, Wu CH, McTernan PM, Adams MWW, Dyer RB. J Am Chem Soc. 2015; 137:4558. [PubMed: 25790178]
28. Schilter D, Rauchfuss TB, Stein M. Inorg Chem. 2012; 51:8931. [PubMed: 22838645]
29. Priego JL, Doerrer LH, Rees LH, Green MLH. Chem Commun. 2000:779.
30. Seiler P, Dunitz JD. Acta Crystallogr, Sect B: Struct Crystallogr Cryst Chem. 1980; 36:2255.
31. Byers LR, Dahl LF. Inorg Chem. 1980; 19:680.
32. Lubitz, W.; van Gastel, M.; Gärtner, W. Nickel and Its Surprising Impact in Nature. Sigel, A.; Sigel, H.; Sigel, RKO., editors. Wiley-VCH; Weinheim, Germany: 2007. p. 279
33. Carroll ME, Chen JZ, Gray DE, Lansing JC, Rauchfuss TB, Schilter D, Volkers PI, Wilson SR. Organometallics. 2014; 33:858. [PubMed: 24803716]
34. Kellers P, Pandelia ME, Currell LJ, Görner H, Lubitz W. Phys Chem Chem Phys. 2009; 11:8680. [PubMed: 20449009]
35. Pandelia ME, Infossi P, Stein M, Giudici-Orticoni MT, Lubitz W. Chem Commun. 2012; 48:823.
36. Kampa M, Pandelia ME, Lubitz W, van Gastel M, Neese F. J Am Chem Soc. 2013; 135:3915. [PubMed: 23402569]
37. Gütlich, P.; Bill, E.; Trautwein, AX. Mössbauer Spectroscopy and Transition Metal Chemistry. Fundamentals and Applications. Springer; Berlin: 2011.
38. Pandelia ME, Bykov D, Izsak R, Infossi P, Giudici-Orticoni MT, Bill E, Neese F, Lubitz W. Proc Natl Acad Sci U S A. 2013; 110:483. [PubMed: 23267108]
39. Surerus KK, Chen M, van der Zwaan JW, Rusnak FM, Kolk M, Duin EC, Albracht SPJ, Muenck E. Biochemistry. 1994; 33:4980. [PubMed: 8161560]
40. Pereira AS, Tavares P, Moura I, Moura JJG, Huynh BH. J Am Chem Soc. 2001; 123:2771. [PubMed: 11456963]
41. Popescu CV, Münck E. J Am Chem Soc. 1999; 121:7877.
42. Zhu W, Marr AC, Wang Q, Neese F, Spencer DJE, Blake AJ, Cooke PA, Wilson C, Schröder M. Proc Natl Acad Sci U S A. 2005; 102:18280. [PubMed: 16352727]

43. Schilter D, Pelmenschikov V, Wang H, Meier F, Gee LB, Yoda Y, Kaupp M, Rauchfuss TB, Cramer SP. Chem Commun. 2014; 50:13469.
44. Pipek J, Mezey PG. J Chem Phys. 1989; 90:4916.
45. Glendening, ED.; Reed, AE.; Carpenter, JE.; Weinhold, F. NBO. University of Wisconsin System; Madison, WI: 1996. version 3.1
46. Pool DH, DuBois DL. J Organomet Chem. 2009; 694:2858.
47. Wang W, Rauchfuss TB, Moore CE, Rheingold AL, De Gioia L, Zampella G. Chem - Eur J. 2013; 19:15476. [PubMed: 24130068]
48. Li Z, Ohki Y, Tatsumi K. J Am Chem Soc. 2005; 127:8950. [PubMed: 15969562]
49. Pandelia ME, Ogata H, Currell LJ, Flores M, Lubitz W. Biochim Biophys Acta, Bioenerg. 2010; 1797:304.
50. Weber K, Krämer T, Shafaat HS, Weyhermüller T, Bill E, van Gastel M, Neese F, Lubitz W. J Am Chem Soc. 2012; 134:20745. [PubMed: 23194246]
51. Chambers GM, Mitra J, Rauchfuss TB, Stein M. Inorg Chem. 2014; 53:4243. [PubMed: 24684697]
52. Tschierlei S, Ott S, Lomoth R. Energy Environ Sci. 2011; 4:2340.
53. Gloaguen F, Rauchfuss TB. Chem Soc Rev. 2009; 38:100. [PubMed: 19088969]
54. Reijerse E, Lendzian F, Isaacson R, Lubitz W. J Magn Reson. 2012; 214:237. [PubMed: 22196894]
55. Stoll S, Schweiger A. J Magn Reson. 2006; 178:42. [PubMed: 16188474]
56. Salzer A, Werner H. Angew Chem, Int Ed Engl. 1972; 11:930.
57. de Beer JA, Haines RJ. J Organomet Chem. 1972; 36:297.
58. Perdew JP. Phys Rev B: Condens Matter Mater Phys. 1986; 33:8822.
59. Becke AD. Phys Rev A: At, Mol, Opt Phys. 1988; 38:3098.
60. Becke AD. J Chem Phys. 1993; 98:5648.
61. Grimme S. J Comput Chem. 2006; 27:1787. [PubMed: 16955487]
62. Zhao Y, Truhlar DG. J Chem Phys. 2006; 125:194101. [PubMed: 17129083]
63. Becke AD. J Chem Phys. 1997; 107:8554.
64. Kamiya M, Tsuneda T, Hirao K. J Chem Phys. 2002; 117:6010.
65. Chai JD, Head-Gordon M. Phys Chem Chem Phys. 2008; 10:6615. [PubMed: 18989472]
66. Dolg M, Wedig U, Stoll H, Preuss H. J Chem Phys. 1987; 86:866.
67. Hariharan PC, Pople JA. Theoret Chim Acta. 1973; 28:213.
68. Hehre WJ, Ditchfield R, Pople JA. J Chem Phys. 1972; 56:2257.
69. Francl MM, Pietro WJ, Hehre WJ, Binkley JS, Gordon MS, DeFrees DJ, Pople JA. J Chem Phys. 1982; 77:3654.
70. Barone V, Cossi M. J Phys Chem A. 1998; 102:1995.
71. Cossi M, Rega N, Scalmani G, Barone V. J Comput Chem. 2003; 24:669. [PubMed: 12666158]
72. Bondi A. J Phys Chem. 1964; 68:441.
73. Floris F, Tomasi J. J Comput Chem. 1989; 10:616.
74. Floris FM, Tomasi J, Ahuir JLP. J Comput Chem. 1991; 12:784.
75. Pierotti RA. Chem Rev. 1976; 76:717.
76. Alecu IM, Zheng J, Zhao Y, Truhlar DG. J Chem Theory Comput. 2010; 6:2872. [PubMed: 26616087]
77. Peng C, Bernhard Schlegel H. Isr J Chem. 1993; 33:449.
78. Peng C, Ayala PY, Schlegel HB, Frisch MJ. J Comput Chem. 1996; 17:49.
79. Page M, McIver JW. J Chem Phys. 1988; 88:922.
80. Koseki S, Gordon MS. J Phys Chem. 1989; 93:118.
81. Solis BH, Hammes-Schiffer S. Inorg Chem. 2011; 50:11252. [PubMed: 21942543]
82. Fernandez LE, Horvath S, Hammes-Schiffer S. J Phys Chem C. 2012; 116:3171.
83. Solis BH, Hammes-Schiffer S. Inorg Chem. 2014; 53:6427. [PubMed: 24731018]

84. Qi XJ, Fu Y, Liu L, Guo QX. Organometallics. 2007; 26:4197.

85. Frisch, MJ.; Trucks, GW.; Schlegel, HB.; Scuseria, GE.; Robb, MA.; Cheeseman, JR.; Scalmani, G.; Barone, V.; Mennucci, B.; Petersson, GA.; Nakatsuji, H.; Caricato, M.; Li, X.; Hratchian, HP.; Izmaylov, AF.; Bloino, J.; Zheng, G.; Sonnenberg, JL.; Hada, M.; Ehara, M.; Toyota, K.; Fukuda, R.; Hasegawa, J.; Ishida, M.; Nakajima, T.; Honda, Y.; Kitao, O.; Nakai, H.; Vreven, T.; Montgomery, JA., Jr; Peralta, JE.; Ogliaro, F.; Bearpark, M.; Heyd, JJ.; Brothers, E.; Kudin, KN.; Staroverov, VN.; Kobayashi, R.; Normand, J.; Raghavachari, K.; Rendell, A.; Burant, JC.; Iyengar, SS.; Tomasi, J.; Cossi, M.; Rega, N.; Millam, JM.; Klene, M.; Knox, JE.; Cross, JB.; Bakken, V.; Adamo, C.; Jaramillo, J.; Gomperts, R.; Stratmann, RE.; Yazyev, O.; Austin, AJ.; Cammi, R.; Pomelli, C.; Ochterski, JW.; Martin, RL.; Morokuma, K.; Zakrzewski, VG.; Voth, GA.; Salvador, P.; Dannenberg, JJ.; Dapprich, S.; Daniels, AD.; Farkas; Foresman, JB.; Ortiz, JV.; Cioslowski, J.; Fox, DJ. Gaussian 09. Gaussian, Inc; Wallingford, CT: 2010. revision D.01

86. Roncaroli F, Bill E, Friedrich B, Lenz O, Lubitz W, Pandelia ME. Chem Sci. 2015; 6:4495–4507.

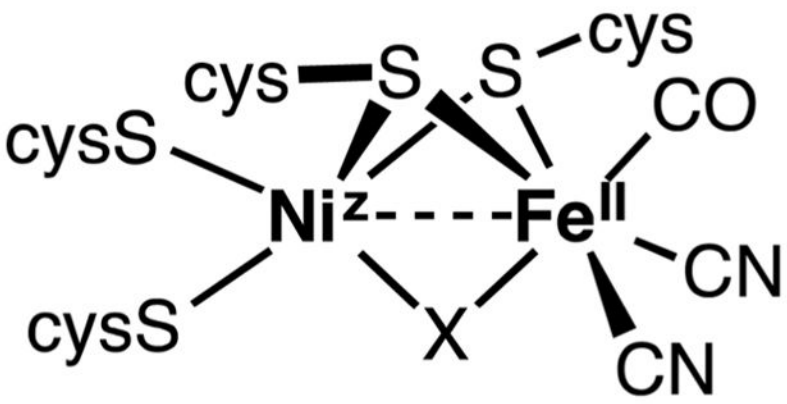

state	*Ni^z*	*X*
Ni-C	Ni^{III}	H
Ni-R	Ni^{II}	H
Ni-SI	Ni^{II}	nil
Ni-L	Ni^{I}	nil

Figure 1.
States of the active site of the [NiFe]-hydrogenases.

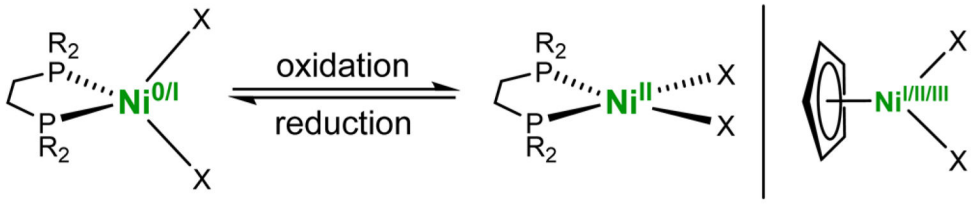

Figure 2.

Nickel diphosphine complexes changing geometry upon the oxidation of tetrahedral $Ni^{0/I}$. The $Ni(C_5H_5)$ center is structurally invariant over three oxidation states.

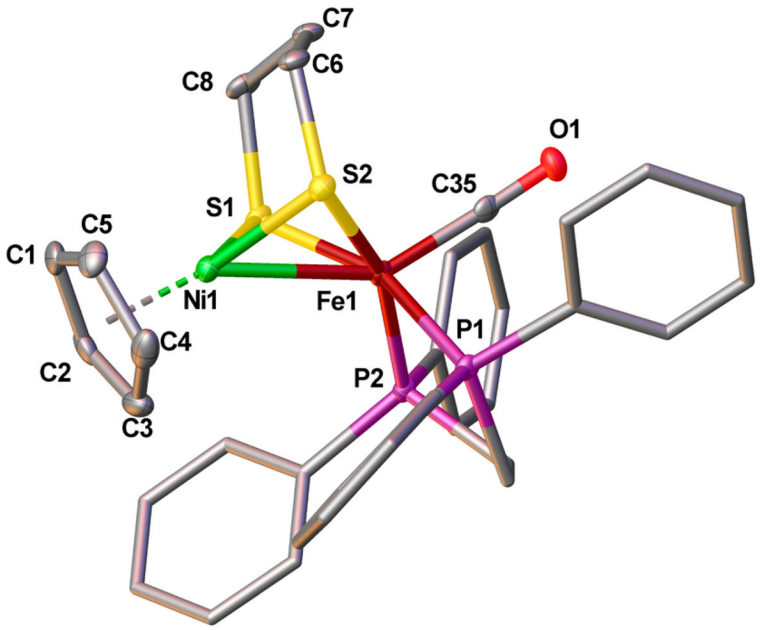

Figure 3.

Solid-state structure of [**1a**]BF_4 shown at the 50% probability level. Hydrogen atoms, counterions, and solvent have been omitted for clarity. Selected bond distances (Å): Ni1–Fe1, 2.5145(4); Ni1–centroid, 1.722(3); Ni1–S_{avg}, 2.1645(7); Fe1–S_{avg}, 2.2208(7); Fe1–C35, 1.757(2); C35–O1, 1.147(2).

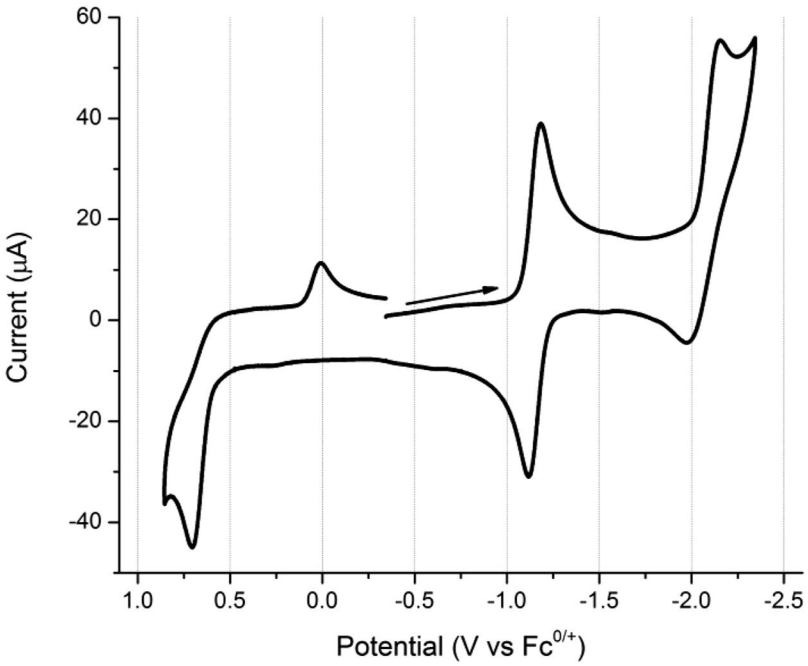

Figure 4.

Cyclic voltammogram of [**1a**]BF_4 at 500 mV s^{-1}. Conditions: ~1 mM in CH_2Cl_2; 100 mM [NBu_4]PF_6; glassy carbon electrode (d = 3 mm); silver wire as the pseudoreference with an internal Fc standard at 0 V; platinum as the counter electrode.

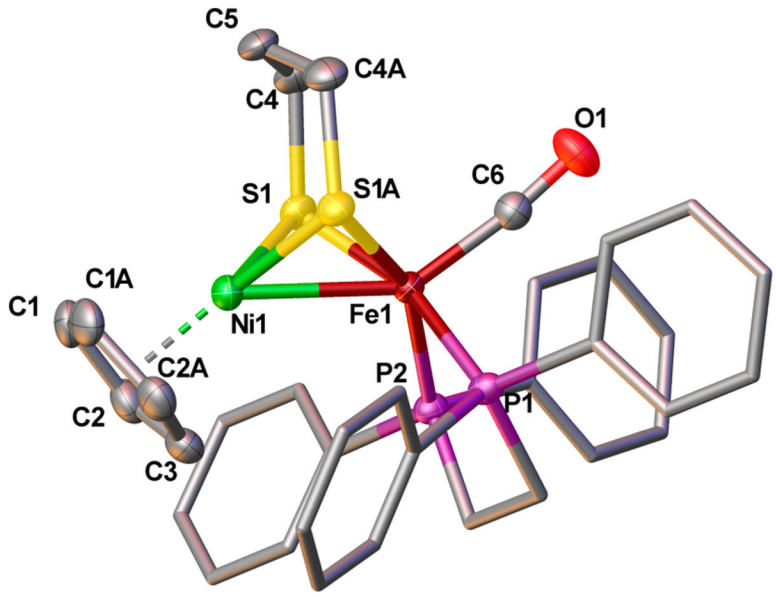

Figure 5.

Solid-state structure of [**1a**]^0 shown at the 50% probability level. Hydrogen atoms and solvent have been omitted for clarity. Selected bond distances (Å): Ni1–Fe1, 2.4593(6); Ni1–centroid, 1.795(3); Ni1–S_{avg}, 2.2772(5); Fe1–S_{avg}, 2.2544(5); Fe1–C6, 1.745(3); C6–O1, 1.159(3).

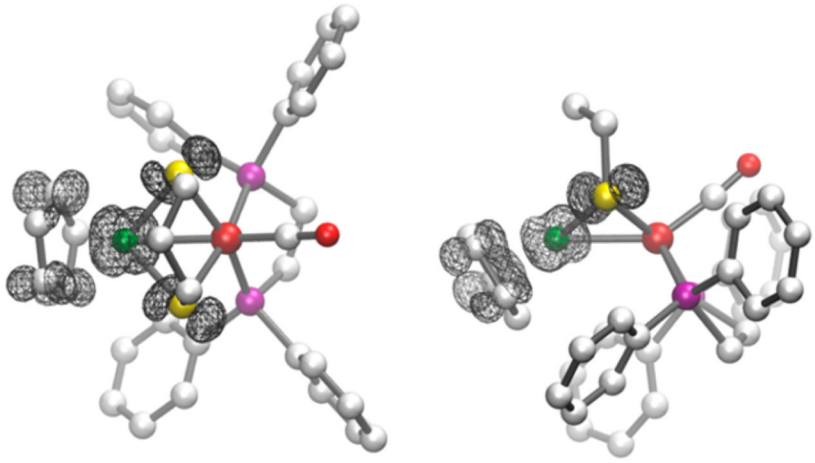

Figure 6.

Views of the isocontour plot of the positive spin density for [**1a**]^{0} from two perspectives. The spin density is localized about the nickel coordination sphere. Color scheme: green, nickel; maroon, iron; yellow, sulfur; purple, phosphorus; red, oxygen; white, carbon. The hydrogen atoms have been removed for clarity.

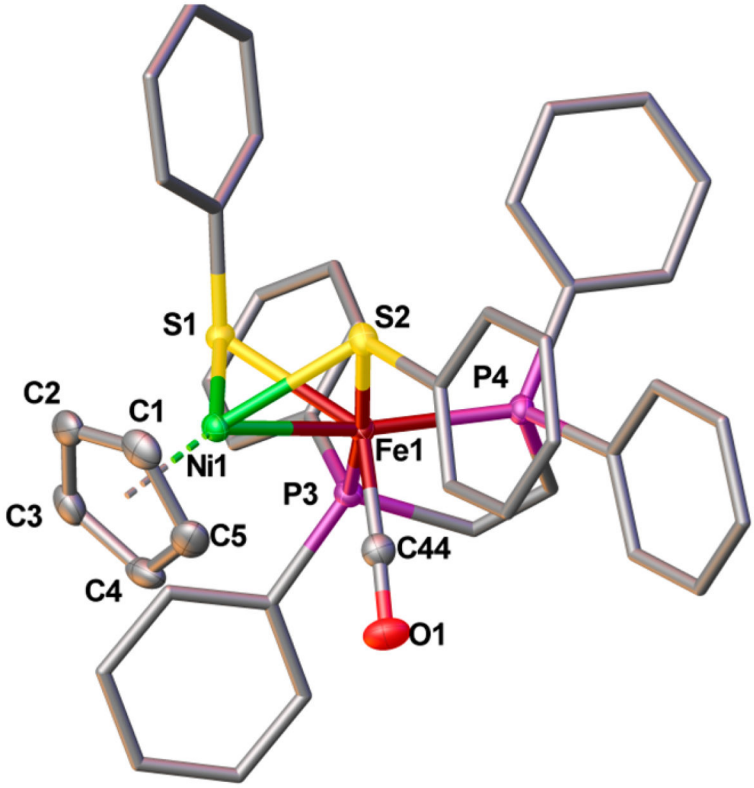

Figure 7.

Solid-state structure of [**2b**]^0 shown at the 50% probability level. Hydrogen atoms and solvent have been omitted for clarity. Selected bond distances (Å): Ni1–Fe1, 2.4594(3); Ni1–centroid, 1.817(2); Ni1–S_{avg}, 2.3067(5); Fe1–S_{avg}, 2.2868(5); Fe1–P_{avg}, 2.1934(5); Fe1–C44, 1.738(2); C44–O1, 1.162(2).

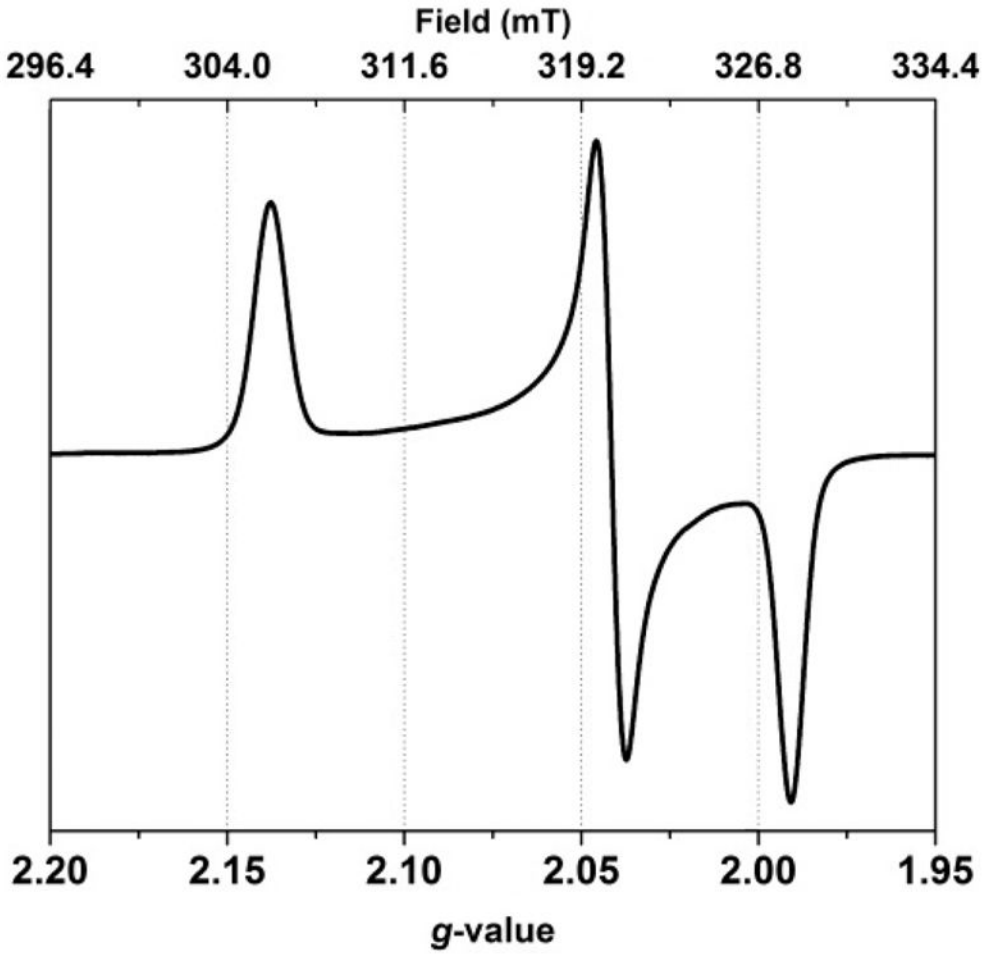

Figure 8.

X-band CW-EPR spectrum of a ~2 mM frozen solution of [**1a**]^0 in 1:1 CH_2Cl_2/THF (110 K).

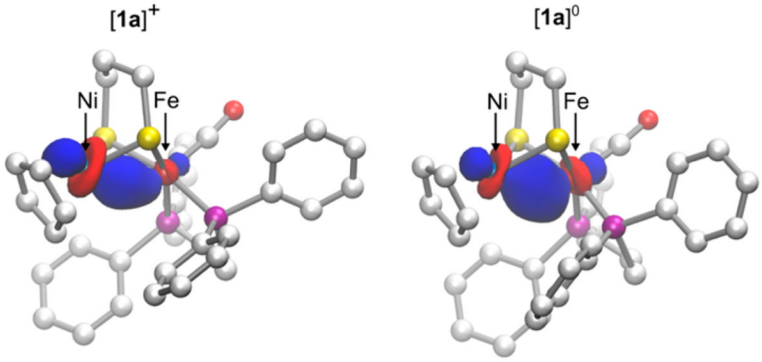

Figure 9.

Pipek–Mezey localized MOs showing the Ni–Fe σ bonds in [**1a**]$^{+}$ and [**1a**]^{0}. The composition of the MO in [**1a**]$^{+}$ is 85% nickel and 15% iron, and the composition of the MO in [**1a**]^{0} is 53% nickel and 47% iron. Only the α orbital is shown for [**1a**]^{0}; however, the β orbital is similar.

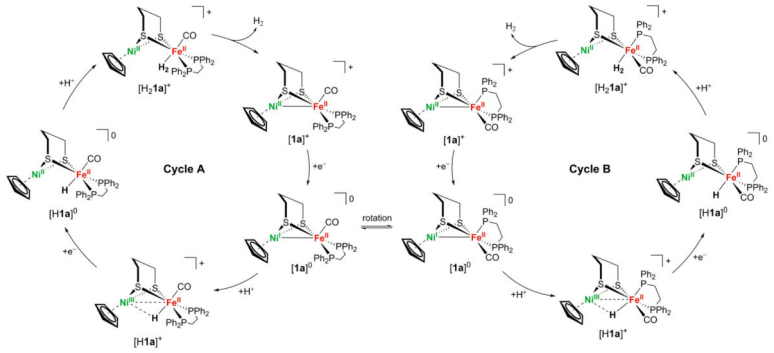

Figure 10.

Proposed mechanism for H_2 production proceeding through two isomers. Cycle A, on the left, proceeds through structures in which the dppe ligand is in the dibasal position. Cycle B, on the right, proceeds through structures in which the dppe ligand spans apical–basal positions. Isomerization of [**1a**]^0, which has the lowest free energy barrier, could lead to a transition between cycles A and B.

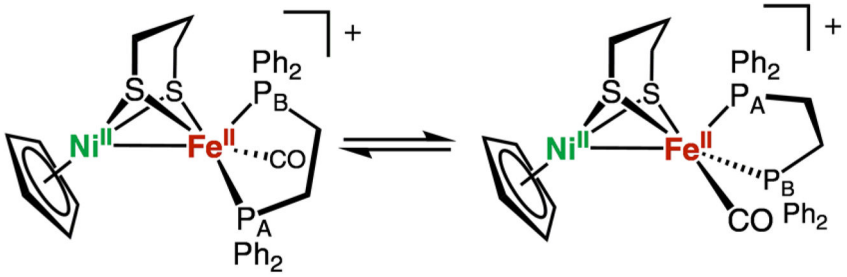

Figure 11.
Representation of the iron-centered rocking motion in [**1a**$^{\mathbf{B}}$]$^{+}$.

$$\textit{Step A:}\ [\mathbf{1a}]^{0} + H^{+} \rightarrow [H\mathbf{1a}]^{+}$$

$$\textit{Step B:}\ [H\mathbf{1a}]^{+} + [\mathbf{1a}]^{0} \rightarrow [H\mathbf{1a}]^{0} + [\mathbf{1a}]^{+}$$

$$\textit{Step C:}\ [H\mathbf{1a}]^{0} + H^{+} \rightarrow [\mathbf{1a}]^{+} + H_{2}$$

Scheme 1.

Table 1

Summary of Models for the Active States of the [NiFe]-Hydrogenase[a]

state	core description	state of the art models	comment
Ni-R	Ni^{II}–H–Fe^{II}	[(diphos)Ni(pdt)(μ-H)$Fe(CO)_2L]^{+}$[14] [(amine)$_2$Ni(SR)$_2$(μ-H)$FeL_3]^{+}$ [15]	models: $d_{Fe-H} < d_{Ni-H}$ enzyme: $d_{Fe-H} > d_{Ni-H}$[16]
Ni-SI	Ni^{II}–_–Fe^{II}	[(diphos)Ni(SR)$_2$Fe(CO)$_2$L$_2$]$^{+}$ [17]	model: six-coordinated iron enzyme: five-coordinated iron[18]
Ni-C	Ni^{III}–H–Fe^{II} [19]	none	no progress
Ni-L	Ni^{I}–_–Fe^{II}	[(diphos)Ni(pdt)Fe(CO)$_2$L]$^{+}$ [20]	model: $Ni^{II}Fe^{I}$ vs enzyme: $Ni^{I}Fe^{II}$ [16]

[a] diphos = $R_2PCH_2CH_2PR_2$; (amine)$_2$(SR)$_2$ = tetradentate diaminodithiolate;[15] L = PR_3 or $P(OR)_3$; pdt^{2-} = $CH_2(CH_2S^{-})_2$.

Table 2

IR Data for Compounds [1a–1d]BF_4 and [2b]BF_4 in a CH_2Cl_2 Solution and the Ni-SI_a State in Selected Organisms

	$\tilde{\nu}_{CO}$ (cm^{-1})	
compound	**expt**	**calc**[a]
$[(C_5H_5)Ni(pdt)Fe(dppe)(CO)]BF_4$ ([**1a**]BF_4)	1943	1948/1946
$[(C_5H_5)Ni(pdt)Fe(dppv)(CO)]BF_4$ ([**1b**]BF_4)	1951	1951/1949
$[(C_5H_5)Ni(Me_2pdt)Fe(dppe)(CO)]BF_4$ ([**1c**]BF_4)	1940	1937/1935
$[(CH_3C_5H_4)Ni(pdt)Fe(dppe)(CO)]BF_4$ ([**1d**]BF_4)	1943	1947/1945
$[(C_5H_5)Ni(SPh)_2Fe(dppv)(CO)]BF_4$ ([**2b**]BF_4)	1956	1959
Ni-SI_a (*Synechocytis SH*)[6]	1947	n/a
Ni-SI_a (*D. vulgaris* Miyazaki F)[32]	1943	n/a
Ni-SI_a (*D. gigas*)[32]	1934	n/a
Ni-SI_a (*A. aeolicus*)[6]	1927	n/a
Ni-SI_a (*Allochromatium vinosum*)[32]	1931	n/a

[a]The first value corresponds to the conformer in which the central CH_2 of the Fe(pdt)Ni core is oriented toward iron, and the second value corresponds to the conformer in which the same CH_2 is oriented toward nickel. The calculations were performed in the absence of BF_4^-.

Table 3

Electrochemical Properties of Compounds [1a–1d]$^{+}$ (V vs $Fc^{+/0}$ in CH_2Cl_2)[a]

compound	$E_{p,ox}$($Ni^{II}Fe^{II}/Ni^{III}Fe^{II}$)	calc[b,c]	$E_{1/2}$($Ni^{II}Fe^{II}/Ni^{I}Fe^{II}$)	calc[b,c]	$E_{p,red}$[d]($Ni^{I}Fe^{II}/Ni^{I}Fe^{I}$)	calc[b,c,d]
[**1a**]BF_4	0.70	0.70	−1.16	−1.16	−2.15	−2.15
[**1b**]BF_4	0.72	0.73	−1.15	−1.12	−2.18	−2.05
[**1c**]BF_4	0.67	0.76	−1.09	−1.16	−2.15	−2.12
[**1d**]BF_4	0.62	0.66	−1.21	−1.23	−2.17	−2.18

[a]For the calculated values, the central CH_2 of the Fe(pdt)Ni core is oriented toward iron and assumed to remain in this orientation upon reduction or oxidation. Additional calculated values corresponding to the same CH_2 being oriented toward nickel, or flipping from iron to nickel, are available in Tables S1 and S2. In all cases, the conformation of the Fe(pdt)Ni core does not affect the potential.

[b][**1a**]BF_4 was used as the reference so the experimental and calculated values agree by construction.

[c]The calculations were performed on the positively charged species in the absence of BF_4^-.

[d]This wave is assigned to a $Ni^{I}Fe^{II}/Ni^{I}Fe^{I}$ couple, where the $Ni^{I}Fe^{I}$ state is an open-shell singlet.

Table 4

IR Data for $\tilde{\nu}_{CO}$ in Compounds [1a–1d]^0 and [2b]^0 in a CH_2Cl_2 Solution

	$\tilde{\nu}_{CO}$ (cm^{-1})	
compound	**expt**	**calc**[a]
[**1a**]^0	1901	1901/1901
[**1b**]^0	1903	1909/1906
[**1c**]^0	1897	1898/1899
[**1d**]^0	1898	1900/1900
[**2b**]^0	1915	1911

[a]The first value corresponds to the isomer in which the central CH_2 of the Fe(pdt)Ni core is oriented toward iron, and the second value corresponds to the isomer in which the same CH_2 is oriented toward nickel.

Table 5

Key Bond Distances (Å) in $[1a]BF_4$ and $[1a]^0$ and the Differences from the Crystal Structures and DFT Calculations

bond	$[1a]BF_4$	calc	$[1a]^0$	calc	experimental difference	DFT difference
Ni–Fe	2.5145(4)	2.566	2.4593(5)	2.508	−0.055	−0.058
Ni–centroid	1.722(3)	1.739	1.795(3)	1.814	+0.073	+0.075
$Ni–S_{avg}$	2.1645(7)	2.168	2.2772(5)	2.259	+0.113	+0.091
$Fe–S_{avg}$	2.2208(7)	2.236	2.2544(5)	2.252	+0.034	+0.016
$Fe–P_{avg}$	2.2256(7)	2.249	2.235(8)	2.236	+0.009	−0.013
Fe–C	1.757(2)	1.721	1.745(3)	1.727	−0.012	+0.006
C–O	1.147(2)	1.171	1.159(3)	1.174	+0.012	+0.003

Table 6

Calculated Spin Densities in Mixed-Valence Species [1a–1d]^0 and [2b]^0 [a]

compound	Ni	Fe	2S	C_5H_5
[**1a**]^0	0.71	−0.17	0.24	0.24
	0.71	−0.19	0.23	0.25
[**1b**]^0	0.69	−0.16	0.22	0.25
	0.69	−0.17	0.22	0.25
[**1c**]^0	0.69	−0.15	0.22	0.24
	0.71	−0.20	0.24	0.25
[**1d**]^0	0.69	−0.17	0.23	0.25[b]
	0.70	−0.19	0.23	0.26[b]
[**2b**]^0	0.72	−0.20	0.20	0.26

[a] For each complex, the first entry corresponds to the isomer in which the central CH_2 of the Fe(pdt)Ni core is oriented toward the Fe center, and the second entry corresponds to the isomer in which the same CH_2 is oriented toward the Ni center.

[b] For [**1d**]^0, this is the spin density over the $CH_3C_5H_4$ ligand.

Table 7

EPR Parameters for Compounds [1a–1d]^0 and [2b]^0 (Frozen CH_2Cl_2/Toluene Solution at 110 K) and the Ni-L State in *Desulfovibrio vulgaris* Miyazaki F[6]

compound	g_1, g_2, g_3
[**1a**]^0	1.991, 2.042, 2.138
[**1b**]^0	1.987, 2.042, 2.134
[**1c**]^0	1.997, 2.044, 2.138
[**1d**]^0	1.987, 2.039, 2.130
[**2b**]^0	1.984, 2.039, 2.143
Ni-L1 (*D. vulgaris*)	2.046, 2.118, 2.296

Table 8

Hyperfine Couplings in $[1a]^0$ from Q-Band ENDOR and Applied Field Mössbauer Measurements

	HFI expt (MHz)		
nucleus	A_1	A_2	A_3
$C_5{}^1H_5$	−4.86	+3.25	−11.25
$CH_2(C^1H_2S)_2$	7.3	4.4	4.36
^{31}P	11.1	11.3	12.7
^{57}Fe	−3.8	−0.73	−0.9

Table 9

Mössbauer Parameters for Compounds [1a–1c]BF_4, [1a–1c]^0, and Ni-SI_a in Regulatory Hydrogenase (RH) from *Ralstonia eutropha*

compound	δ (mm s^{-1})	ΔE_q [a] (mm s^{-1})	η
[**1a**]BF_4	0.11	1.15	
[**1b**]BF_4	0.11	1.10	
[**1c**]BF_4	0.12	0.87	
[**1a**]^0	0.14	−0.73	0.13
[**1b**]^0	0.13	−0.72	
[**1c**]^0	0.13	−0.76	
Ni-SIa *RH* (*R. eutropha*)[86]	0.10	1.60	

[a] ΔE_Q signs for [**1a**–**1c**]^0 are obtained from magnetic Mössbauer spectra.

Table 10

Spin Densities and Bond Lengths (Å) of $[1a]^0$, $[H1a]^+$, and $[H1a]^0$ [a]

	$[1a]^0$		$[H1a]^+$		$[H1a]^0$	
	isomer A	**isomer B**	**isomer A**	**isomer B**	**isomer A**	**isomer B**
ρ(Ni)	0.71	0.70	0.45	0.42	0.00	0.00
ρ(Fe)	−0.19	−0.16	0.24	0.29	0.00	0.00
ρ(2S)	0.23	0.23	0.12	0.09	0.00	0.00
ρ(C_5H_5)	0.25	0.23	0.18	0.16	0.00	0.00
d(Ni–Fe)	2.53	2.47	2.60	2.59	3.01	2.85
d(Ni–H)	n/a	n/a	1.80	1.79	2.44	2.05
d(Fe–H)	n/a	n/a	1.61	1.58	1.54	1.53

[a] For these calculations, the central CH_2 of the Fe(pdt)Ni core is oriented toward the nickel center. An analogous table for the cases where the same CH_2 is oriented toward the iron center is provided in the Table S10.

Table 11

Calculated Reaction Free Energies and Free Energy Barriers (kcal mol^{-1}) for Isomerization of Dibasal to Apical–Basal Isomers for $[1a]^0$ and Its Derivatives in the Proposed Catalytic Cycle[a,b,c]

compound	$\Delta G°$	$\Delta G^{‡}$
$[\mathbf{1a}]^0$	0.48	11.76
$[H\mathbf{1a}]^+$	2.21	20.84
$[H\mathbf{1a}]^0$	5.18	25.64
$[H_2\mathbf{1a}]^+$	9.86	30.03
$[\mathbf{1a}]^+$	2.03	21.54

[a] See Figure 10 for structures of all species.

[b] For the isomerization considered here, the central CH_2 of the Fe(pdt)Ni core is oriented toward the nickel center. The calculated values corresponding to the cases where the same CH_2 is oriented toward the iron center are provided in Table S9.

[c] The potential energy surface was found to be relatively flat along the isomerization pathway, leading to relatively small imaginary frequencies for the TSs.